Evolution of a Surge Cycle of the Bering-Bagley Glacier System from Observations and Numerical Modeling

Thomas Trantow[1] **and Ute C. Herzfeld**[1,2]

[1]Department of Electrical, Energy and Computer Engineering, University of Colorado, Boulder, Colorado, USA
[2]Cooperative Institute for Research in Environmental Sciences, University of Colorado, Boulder, Colorado, USA

Key Points:

- Using a full-Stokes approach and satellite observations, the dynamic, geometric and hydraulic evolution of the BBGS during surge is modeled
- Local bed topography controls the formation of reservoir areas, slows water drainage, and retains water in trigger areas during quiescence
- A new friction law for the surge phase is introduced based on observed properties of kinematic surge waves in the BBGS

Corresponding author: Thomas Trantow, `trantow@colorado.edu`

Abstract

The recent surge of the Bering-Bagley Glacier System (BBGS), Alaska, in 2008-2013 provided a rare opportunity to study surging in a large and complex system. We simulate glacier evolution for a 20 year quiescent phase, where geometrical and hydrological changes lead to conditions favorable for surging, and the first two years of a surge phase where a surge-front propagates through the system activating the surging ice. For each phase, we analyze the simulated elevation-change and ice-velocity pattern, and infer information on the evolving basal drainage system through hydropotential analysis. During the quiescent phase simulation, several reservoir areas form at locations consistent with those observed. Up-glacier of these reservoir areas, water drainage paths become increasingly lateral and hydropotential wells form indicating an expanding storage capacity of subglacial water. These results are attributed to local bedrock topography characterized by large subglacial ridges that act to dam the down-glacier flow of ice and water. Based on the BBGS's end-of-quiescence state, we propose several surge initiation criteria to predict when the system is set to surge. In the surge simulation, we model surge evolution through Bering Glacier's trunk by implementing a new friction law that mimics a propagating surge-wave. Modeled surge velocities share spatial patterns and reach similar peaks as those observed in 2008-2010. As the surge progresses through the glacier, drainage efficiency further degrades in the active surging zone from its already inefficient, end-of-quiescence state. Satellite observations from 2013 indicate hydraulic drainage efficiency throughout the glacier was restored after the surge had ended.

Plain Language Summary

The recent surge of the Bering-Bagley Glacier System (BBGS), Alaska, in 2008-2013 provided a rare opportunity to study surging in a large and complex system. A surge glacier cycles between a long period of normal flow and a short period of accelerated flow where large-scale deformations, such as crevasses, occur. We use a numerical model to simulate glacier evolution for both the quiescent phase and the initial surge phase of the BBGS. For each phase, we analyze the simulated elevation-change and ice-velocity, and infer information on the evolving hydraulic drainage system. During the quiescent phase simulation, mass build-ups form at locations consistent with those observed and water drainage paths become less efficient with expanding storage capacity of subglacial water. These results are attributed to local bedrock topography characterized by large subglacial ridges that act to dam the down-glacier flow of ice and water. In the surge simulation, we model surge evolution through Bering Glacier by implementing a new friction law that mimics a propagating surge-wave. As the surge progresses through the glacier, drainage efficiency further degrades in the areas of fast-moving ice. Satellite observations from 2013 indicate hydraulic drainage efficiency throughout the glacier was restored after the surge had ended.

1 Introduction

The Bering-Bagley Glacier System (BBGS) in southeast Alaska stretches nearly 200 km in length and covers an area greater than 5000 km^2 making it the largest temperate glacier system in the world (B. F. Molnia & Post, 2010) (see Figure 1). The BBGS is likely the largest surge glacier system outside of the major ice sheets with surge events occurring every 20-25 years (Post, 1972; B. F. Molnia & Post, 2010; Lingle et al., 1993; B. Molnia & Post, 1995; U. C. Herzfeld & Mayer, 1997; U. Herzfeld, 1998; B. Molnia & Williams, 2001; D. R. Fatland & Lingle, 1998; Mayer & Herzfeld, 2000; B. F. Molnia, 2008; D. R. Fatland & Lingle, 2002; Roush et al., 2003; Fleischer et al., 2010; Josberger et al., 2010; R. A. Shuchman et al., 2010; R. Shuchman & Josberger, 2010). The most recent surge of the BBGS in 2008-2013 (U. C. Herzfeld et al., 2013; Burgess et al., 2013) provides a rare opportunity to investigate surging in a large and complex glacier system.

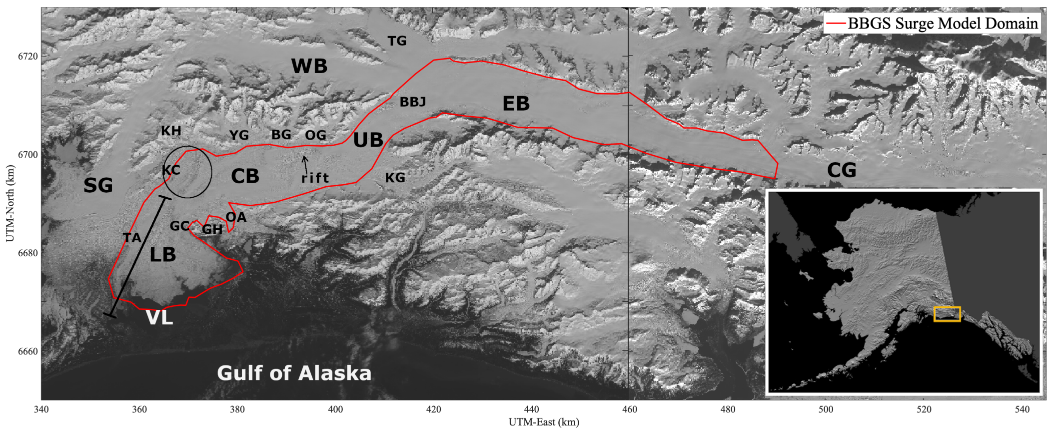

Figure 1. Key features in and around the Bering Bagley Glacier System including the numerical model domain. The red line marks the domain of the BBGS model. LB – Lower Bering Glacier, also referred to as the "lobe area" or the Bering Lobe, CB – Central Bering Glacier; UB – Upper Bering Glacier; EB – Eastern Bagley Ice Field; BBJ – Bering-Bagley Junction; WB – Western Bagley Ice Field; SG – Steller Glacier; CG – Columbus Glacier; VL – Vitus Lake; GH – Grindle Hills; GC – Grindle Corner; KH – Khitrov Hills; TG – Tana Glacier; YG – Yushin Glacier; BG – Betge Glacier; OG – Ovtsyn Glacier; KG – Kuleska Glacier; OA – Overflow Area also known as the Kaliakh Lobe; TA – Tashalish Arm (indicated by black line segment); KC – Khitrov Crevasses (circled in black). The rift is indicated by a black arrow in Upper Bering. The Eastern and the Western Bagley Ice Fields together are also referred to simply as the Bagley Ice Field (BIF). Note the combination of Upper and Central Bering Glacier constitute Bering Glacier's "trunk" and the imaginary line connecting the Khitrov Hills to the Grindle Hills across Bering Glacier is referred to as Khitrov-Grindle Line. The BBGS is surrounded by the Chugach-Saint Elias mountain range. Background images from Landsat-8 acquired on 28 April 2013 (left) and 7 March 2014 (right). Reference image in lower right: U.S. Geological Survey Map I-2585.

1.1 Glacier Surging

A surge-type glacier cycles quasi-periodically between a long quiescent phase of regular flow speeds and gradual retreat, and a short surge phase when ice flow accelerates 10-100 times its normal velocity. During the quiescent phase, the geometry of a surge-type glacier changes by thickening in particular areas and thinning in others, resulting in regions of overall steepening often accompanied by observed "bulges" at the glacier surface (Meier & Post, 1969; Fowler, 1987; Raymond, 1988; U. C. Herzfeld & Mayer, 1997; U. Herzfeld, 1998; U. C. Herzfeld et al., 2013). This mass redistribution leads to definitions of *reservoir areas*, defined as areas of general thickening during the quiescent phase, and *receiving areas* where mass is transferred during the surge phase.

An observed bulge often coincides with the surge "front" that propagates as a kinematic wave down-glacier with resulting effects that propagate up-glacier as well. The down-glacier propagation is thought to change the basal hydrological conditions, perhaps through increased driving stress, leading to increased water pressure, reduced friction and thus increased basal motion (Fowler, 1987) that accounts for nearly all the observed dynamics during a surge (Cuffey & Paterson, 2010). As the wave moves down-glacier, it activates the increased basal motion for a section of the glacier (Fowler, 1987), leading to accelerating (surging) ice within this "activation zone". The evolving bounds of the activation zone are given by a leading edge coinciding with the surge front and a trailing edge (Fowler, 1987). Studies on smaller surge-glaciers find that the entire glacier can be active at the same time once the activation-wave reaches the terminus, e.g. Finsterwalderbreen in Robin and Weertman (1973) whose length is ≈ 14 km. Turrin et al. (2013) maps the kinematic wave for the latest BBGS surge and suggest that the activated portion of the glacier extends up to the Bering-Bagley Junction (BBJ), near their proposed surge-trigger area.

Smaller-scale acceleration events are known to occur during the quiescent phase of some surge-glaciers leading to temporary relaxation of the increased driving force that accompanies surface steepening (Meier & Post, 1969; Raymond, 1987; Harrison & Post, 2003). However, during the true surge phase, a rapid and full-scale acceleration event redistributes ice throughout the entire glacier system resulting in drastic elevation changes, with rapid thinning of the former reservoir areas, thickening in the receiving areas and drawdowns along the margins of the glacier (Meier & Post, 1969; Raymond, 1987; Harrison & Post, 2003; Fowler, 1987, 1989). Heavy and wide-spread crevassing also occurs during the surge phase, indicative of rapid deformation, horizontal and vertical displacement of ice and sudden changes in flow speeds.

Most studies on surges are conducted on smaller glaciers that consist of a single reservoir area in the accumulation zone and a single reservoir area down-glacier near the terminus, e.g., Variegated Glacier, Alaska (W. Kamb et al., 1985; Eisen et al., 2005; Jay-Allemand et al., 2011a) or Black Rapids Glacier, Alaska (Raymond et al., 1995; Heinrichs et al., 1996; D. Fatland et al., 2003). However, as we show in this study, a large and complex glacier system like the BBGS can consist of multiple reservoir and receiving areas which can lead to a complicated picture of the surge evolution. Moreover, a complex glacier system can have both surge-type and non-surge-type parts, with different processes, such as surge initiation and re-initiation, occurring in different locations and at different times (U. Herzfeld, 1998; U. C. Herzfeld et al., 2013). The BBGS shares this property of complexity with sections of the Greenland and Antarctic ice sheet margins, where surge-type glaciers are found neighboring non-surge-type glaciers and accelerating outlet glaciers (Jiskoot, 1999; U. C. Herzfeld, 2004; Sevestre et al., 2015). Thus, the study of the BBGS surge provides extra layers of insight into the complex glacier acceleration found along the ice sheet margins, compared to the more commonly studied surges of smaller mountain glaciers.

In general, surge-type glaciers are present in distinct climatic environments and tend to have greater areas, longer lengths and lower surface gradients than non-surge-type glaciers (Sevestre et al., 2015; Benn et al., 2019). While internal dynamics are believed to govern glacial surging, climatic effects, including mass balance and even weather, are known to effect surge initiation, termination, and the length of each phase in the surge-cycle for some glaciers (Harrison & Post, 2003). Murray et al. (2003) point out there may not be a single surge mechanism due to observed differences between surge glaciers found in Alaska and those found in Svalbard. Svalbard, or Arctic, glacier systems contain polythermal ice while glaciers in southeast Alaska comprise entirely of temperate ice, that is, ice at or near the melting point. The BBGS is an ideal prototype of the Alaskan-type surge. During the summer in southeast Alaska, warmer temperatures induce surface melting throughout the glacier system. The meltwater is transferred to the base through englacial tunnels, or moulins, thus requiring the formation of drainage system at the ice/bedrock interface to transfer the water down-glacier.

Alaskan-type surges are associated with rapid changes in the subglacial hydraulic drainage system (W. Kamb et al., 1985). The system may consist of flow through channels or linked-cavities in the basal ice or bedrock (hard-bed case), or through a deformable sediment (or till) layer at the ice-bed interface (soft-bed case) (Weertman, 1972; Lliboutry, 1968; Shoemaker, 1986; W. B. Kamb, 1987; Fowler, 1987; Murray, 1997; Björnsson, 1998; Truffer et al., 2000). In the case of a hard bed, sliding of the ice over the rigid bedrock constitutes the dominant process of rapid glacier flow while the soft-bed case implies deformation of a subglacial till layer. Observations of basal morphologies indicate most Alaskan glaciers have an underlying till layer (Harrison & Post, 2003). While the exact physics relating to surge initiation and motion are different between the two cases, a reduction in the hydraulic drainage efficiency would result in increased basal water pressures and increased basal sliding speeds in both cases (Harrison & Post, 2003). In the current study, we do not distinguish the bed-type, and instead focus on water pressure and drainage efficiency inferred from hydropotential calculated at the ice-bed boundary and its relation to basal motion via a friction law.

A surge is accompanied by a rapid switch from a generally efficient drainage system (EDS), characterized by low-subglacial water pressures, to an inefficient drainage system (IDS) with high basal water pressures (W. Kamb et al., 1985; Harrison & Post, 2003). At any given time, a surge-type glacier can be a tightly-coupled combination of both an EDS and an IDS (Björnsson, 1974; Shoemaker & Leung, 1987; Björnsson, 1998; Boulton et al., 2007; Magnússon et al., 2010). During quiescence however, the glacier system is almost entirely comprised of an EDS. A secularly evolving glacier geometry over the course of quiescence leads to conditions that initiate a surge through destruction of the EDS with a transition to a persistent IDS during the surge phase (W. B. Kamb, 1987; Harrison & Post, 2003). A key difference between the two systems is how they react to an increase in water discharge to the base. In this case, basal water pressures increase throughout an IDS whereas an EDS will increase its capacity to store the increased discharge leading to lower pressures (de Fleurian et al., 2018). A hydraulic system must be able to maintain high water pressures for some time in order for the IDS to persist and grow thus initiating a full-scale surge (W. B. Kamb, 1987).

Subglacial and englacial water storage contribute to the switching and persistence of hydraulic regimes (Harrison & Post, 2003). The destruction of an EDS traps water that would have normally drained allowing the rapid increase of basal water pressure associated with an IDS. The persistence of an IDS, and its expansion to more parts of the glacier system, depends on the amount of stored water available to maintain high basal water pressures. In this paper, we show that over the course of quiescence, Bering Glacier evolves the capacity to store more and more englacial and subglacial water through the development of hydropotential wells and longer, more-transverse drainage paths, thus complicating the concept of an EDS as described above. We also investigate the progression of the surge as it relates to an expanding IDS, maintained by exacerbated drainage inefficiencies.

Finally, stored water during a surge is reflected by the occurrence of large outburst floods at the glacier terminus, which is accompanied by surge termination and a return to normal flow, lower water pressures and an EDS (Humphrey & Raymond, 1994; Harrison & Post, 2003). Such outburst floods have been observed for previous surges of the BBGS (D. R. Fatland & Lingle, 1998). The current study uses CryoSat-2 elevation data to demonstrate that after a surge of the BBGS, the glacier drainage reverts to a more efficient drainage system with less capacity to store subglacial and englacial water.

1.2 Observations of the Recent BBGS Surge

The onset of the latest major surge event in Bering Glacier occurred in early 2011 affecting mostly Lower and Central Bering Glacier (Figure 2) (U. C. Herzfeld et al., 2013), while lesser surge activity was observed near in Upper Bering Glacier after the opening of a giant longitudinal rift (Figure 2(a-b)) where elevated ice-velocities were observed in 2008 (U. C. Herzfeld et al., 2013; Burgess et al., 2013). This rift, also observed during the 1993-1995 surge (U. Herzfeld, 1998), reached 60 m in depth upon forming and grew in size throughout the surge reaching nearly 200 m in width and 10 km in length by 2013 (U. C. Herzfeld et al., 2013; Trantow, 2020).

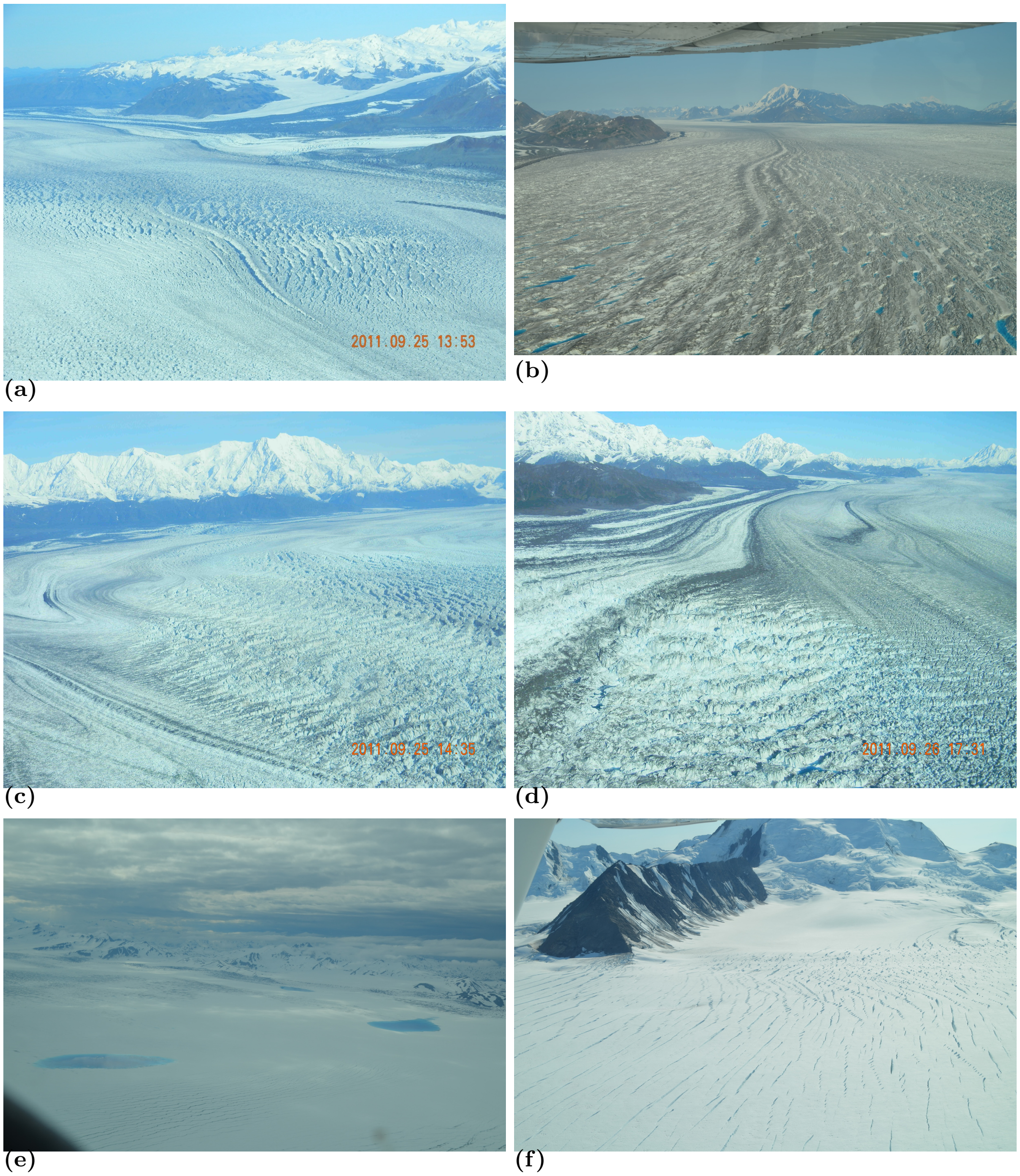

Figure 2. Imagery from the airborne campaign flights over Bering Glacier 2011-2013. (a) Large longitudinal rift in Upper Bering Glacier along the northern branch in September 2011(looking down-glacier) and (b) in August 2013 with water in the surrounding crevasse field (looking up-glacier), (c) upper Tashalish Arm (September 2011), (d) Khitrov Crevasses (foreground) formed during the second stage of the surge in early-2011 (September 2011), (e) three supraglacial lakes in Central Bering Glacier as observed in July 2012, and (f) en-échelon crevasses along the southern margin of the upper Bagley Ice Field (August 2013).

Surface speeds in late 2007 and early 2008 were around 1 m/day (365 m/a) in the Bagley Ice Field and Upper-Bering Glacier (LeBlanc, 2009). Between September 2008 and February 2009 the BBGS accelerated progressively from the BBJ to the lower-mid glacier right above the overflow area (Turrin et al., 2013; Burgess et al., 2013). The maximum recorded velocity was 7 m/day (2555 m/a) near mid-glacier but peak speeds might have been even higher (Burgess et al., 2013). In early 2010, surface speeds in Lower and Central Bering Glacier returned close to normal quiescent speeds and velocities in the lower Bagley Ice Field and Upper Bering were measured at around 2 m/d (720 m/a).

In early 2011, Bering Glacier's dynamics changed to a full-scale surge resulting in crevassing throughout a large portion of the glacier (U. C. Herzfeld et al., 2013). The recently heightened reservoir area, i.e. a bulge, in the lower-central Bering, observed by (U. C. Herzfeld et al., 2013) and (Burgess et al., 2013), transferred its mass down-glacier along the northern branch of the flow regime to the lower Tashalish arm area (the westernmost part of the Bering lobe, Figure 2(c)). The former reservoir area experienced surface lowering of 40-70 meters while the receiving area gained 20-40 meters of surface elevation by fall 2011 (U. C. Herzfeld et al., 2013). The bulge collapse resulted in the formation of large surge crevasses in the Khitrov crevasse field (Figure 2(d)). The thickening continued to move downstream until it reached the terminus, where it extended 2-4 km (Turrin et al., 2013).

There were very few measurements of velocity during 2011 provided by Burgess et al. (2013), but one 11 day interval in the beginning of July showed a peak velocity of 9 m/day (3285 m/a) near the boundary of Upper and Central Bering Glacier. Burgess et al. (2013) provided no velocity measurements in the Lowerf Bering Glacier. Velocity measurements of Lower Bering from Trantow and Herzfeld (2018) revealed that surge velocities in early 2011 reached at least 21 m/day.

Aerial observations from the campaigns of U. C. Herzfeld et al. (2013) revealed that the surge continued to induce significant effects throughout the glacier system in 2012 and 2013. The presence of large supraglacial lakes in the summer of 2012 in Central Bering (Figure 2(e)) indicated that the glacier remained in a state of inefficient drainage. By 2013 most of the dynamical activity in Bering Glacier had ceased though the effects of the surge were still being felt in the Bagley Ice Field as demonstrated by the opening of fresh en-échelon crevasses (Figure 2(f)). These characteristic en-échelon crevasses form when the kinematic energy from the surge causes deformation at pre-existing weaknesses in the ice (crevasses) caused by the local topography (U. C. Herzfeld & Mayer, 1997). A more comprehensive documentation of observations from latest surge is given in Chapter 2 of Trantow (2020).

While it is not simple and obvious to assign the time of surge initiation and surge termination in a complex glacier system like the BBGS, for the purposes of this study we presuppose that the most recent surge initiated in early-2008 in Upper Bering near the rift area. The surge from 2008-2010 constitutes the first, or initial surge phase. We then refer to the surge activity in 2011-2013 as the second, or major, surge phase as most of the dynamical activity occurred during this time (U. C. Herzfeld et al., 2013).

2 Approach

In this study we conduct prognostic simulations using the model introduced in Trantow and Herzfeld (2018) to investigate changes that occur in the BBGS during a quiescent and early-surge phase. For each phase, we analyze mass redistribution within the glacier system to help estimate changes in hydrological drainage characteristics, which are known to play a major role in flow behavior and state switching in a surge-type glacier. The most important aspect of our ice-flow model is the treatment of the ice-bed boundary, that is, the input bedrock topography and the prescribed friction law (Section 3.2.2). While the input bedrock topography remains fixed throughout the surge cycle, parameters of the basal friction law are different for each phase and will spatiotemporally evolve during the surge phase reflecting a passing surge-wave (Section 3.2.2.2).

The BBGS model was built using the finite element software Elmer/Ice (Gagliardini et al., 2013) and has been used in previous diagnostic studies that used a crevasse-based approach to constrain unknown model parameters during the early-2011 phase of the latest BBGS surge (Trantow & Herzfeld, 2018). Our previous work focused on synthesizing the model-data connection using a variety high-quality data inputs, which includes observations of surface height (Trantow & Herzfeld, 2016), velocity, crevasse location and crevasse orientation (Trantow & Herzfeld, 2018), and showed that model results and parameter optimization were robust to relative uncertainties in the observational inputs (Trantow et al., 2020). In the current study, we switch to prognostic modeling by performing longer transient simulations while using the same optimized model parameterization and high quality observational data sets derived in our previous studies.

With relatively high resolution bedrock and ice-surface topography inputs, our approach for modeling basal friction during quiescence and the surge phase allows glacier geometry to explain as much of the spatial variability in the glacier's dynamics as possible. That is, we do not fit friction parameters based on observed velocity, e.g. (Larour et al., 2014), and instead attempt to keep parameterization as simple as possible in order to adequately capture observed dynamic behavior. Discrepancies in modeled and observed behaviors informs the next step up in complexity with regards to the basal friction law in both the quiescent and surge phases (Section 4.4).

Our modeling approach here does not include seasonal variability but instead looks at inter-annual (secular) trends. For example, we enforce an observed mean annual surface mass balance (SMB) uniformly throughout the entire model duration. While seasonal changes in glacial water are known to play a role in the intra-annual timing of surges (Raymond, 1987), our analysis will focus on inter-annual and seasonally-independent changes in hydrological characteristics of the subglacial drainage system, which govern the approximate length of the surge cycle phases. That is, we focus on modeling dynamics resulting from internal characteristics of the glacier system, which are known to determine whether a glacier is or is not a surge-type glacier. If surging depended strongly on seasonal components such as precipitation, then we would expect neighboring glaciers to have similar dynamic responses as those observed for the BBGS. For example, neighboring Steller Glacier (see Figure 1) is not known to surge. In fact, Trantow (2020) has shown that local precipitation and temperature anomalies have no correlation with the timing and duration of the last three BBGS surges.

In part due to computational limitations at the time of analysis, we simulate the quiescent phase and initial surge phase of the BBGS cycle separately. We use observed geometry in 2016, when the BBGS is in a fully quiescent state, to initialize the 20 year quiescent simulation. The end-of-quiescence geometry is then used to initialize the 2-year early-surge phase simulation. While the two phases are simulated separately, the geometric and hydrologic characteristics of the BBGS at the end of quiescence inform proposals for surge initiation criteria that may be used in future simulations that aim to simulate the entire BBGS surge cycle in a single run. Due to the computational resources required to simulate the entire surge phase using the full-Stokes representation, we rely on satellite observations to interpret the second surge phase that last occurred in 2011-2013 rather than explicit modeling.

Our successful model simulations provide valuable insight into the surge of the BBGS, which we cover in this paper. After introducing the salient model aspects in Section 3, we analyze the simulation of results of the quiescent phase in Section 4 and the early-surge phase in Section 5. For each phase, we investigate (1) the mass redistribution and geometrical changes in the glacier system, (2) the hydrological implications of those changes, and (3) how these results can improve our model representations. Observations of surface height, velocity and mass balance help guide and validate our modeling efforts throughout. In addition, we propose methods for initiating a surge in Section 5.1 while in Sections 5.3 and 5.4 we use velocity maps and CryoSat-2 observations from the end of the latest surge in 2013 to investigate the state of the glacier system at the end of the surge phase.

3 Numerical Model

For numerical experiments of ice flow and crevassing, we have created a 3D finite element model of the BBGS using the open-sourced software Elmer/Ice (Gagliardini et al., 2013). The BBGS model is covered in depth in Trantow and Herzfeld (2018) in relation to diagnostic surge experiments and model-data connection. In the current section, we cover only the salient model details and introduce several new aspects required for the longer prognostic simulations performed for this paper.

3.1 Flow Law for Temperate Ice

As mentioned previously, we employ the full-Stokes representation to model the complex glacier dynamics of the surging BBGS. The full-Stokes equations utilize conservation laws to describe the flow of ice via internal deformation as forced by gravity. They have no simplifying assumptions on the stress regime, in contrast to the common Shallow Ice (SIA) or Shallow Shelf (SSA) approximations. Stokes flow simplifies the more general Navier-Stokes equations for viscous fluid flow by assuming the inertial forces are negligible in comparison to viscous forces. Momentum conservation is given by

$$\nabla \cdot \boldsymbol{\sigma} + \rho \boldsymbol{g} = \nabla \cdot (\boldsymbol{\tau} - p\boldsymbol{I}) + \rho \boldsymbol{g} = 0, \qquad (1)$$

and conservation of mass is given by

$$\nabla \cdot \boldsymbol{u} = tr(\dot{\boldsymbol{\epsilon}}) = 0, \qquad (2)$$

where $\boldsymbol{\sigma} = \boldsymbol{\tau} - p\boldsymbol{I}$ is the Cauchy stress tensor, $\boldsymbol{\tau}$ the deviatoric stress tensor, p the pressure, ρ the ice density, $\boldsymbol{g} = (0, 0, -9.81)$ the gravity vector, $\boldsymbol{u}$ the velocity vector and $\dot{\boldsymbol{\epsilon}} = \frac{1}{2}(\nabla \boldsymbol{u} + (\nabla \boldsymbol{u})^T)$ the strain-rate tensor.

The relation between stress and the internal flow of ice is given by Glen's Flow Law,

$$\boldsymbol{\tau} = 2\eta \dot{\boldsymbol{\epsilon}}, \qquad (3)$$

where η is the effective viscosity defined as,

$$\eta = \frac{1}{2} A^{-1/n} \dot{\epsilon}_e^{(1-n)/n}, \qquad (4)$$

where $\dot{\epsilon}_e$ is the effective strain-rate and n the Glen exponent, set as $n = 3$ for all experiments in this study, which is a well established value for temperate glacier flow (Greve & Blatter, 2009; Cuffey & Paterson, 2010). The rate-factor $A = A(T')$ is a rheological parameter, which depends on the ice temperature via an Arrhenius law, is given by

$$A(T') = A_0 exp(\frac{-Q}{RT}), \qquad (5)$$

where Q is the activation energy, R the universal gas constant, A_0 a pre-exponential constant, and T' the temperature relative to the pressure melting point. The BBGS is a temperate glacier, implying the temperature of most of the ice is at or near the pressure melting point throughout the entire year. Therefore, we employ an isothermal assumption with ice temperature set to 0°C resulting in a rate-factor of $A(0°C) = 75.7 MPa^{-3} a^{-1}$.

3.2 Boundary Conditions

3.2.1 Ice/Atmosphere Boundary

At the surface of the glacier, a stress-free boundary condition is employed

$$\boldsymbol{\sigma n_s} = -p_{atm}\boldsymbol{\sigma} \approx 0 \tag{6}$$

which assumes the atmospheric pressure, p_{atm}, acting as a stress normal to the ice surface, $\boldsymbol{\sigma n_s}$, is negligible with regards to its effect on ice flow. We also allow our glacier surface to freely evolve in order to investigate elevation change. The upper free surface is governed by an advection equation

$$\frac{\partial z_s}{\partial t} + u_s \frac{\partial z_s}{\partial x} + v_s \frac{\partial z_s}{\partial y} - w_s = a_s, \tag{7}$$

where $\boldsymbol{u_s} = (u_s, v_s, w_s)$ is the surface velocity vector given by the Stokes equation (Equation 2) and a_s is the accumulation or ablation component prescribed in the direction normal to the surface (Gagliardini et al., 2013). The accumulation and ablation term we apply in our BBGS simulations is given by observations of mean surface mass balance with respect to elevation from Tangborn (2013) from 1951 to 2011 and from surface mass balance (SMB) observations of Alaskan glaciers form Larsen et al. (2015) (see Section 3.4).

Initial ice-surface topography for the quiescent phase is derived from CryoSat-2 data using waveform analysis that combines a swath-processing technique together with the Threshold First Maximum Retracking Algorithm (TFMRA) (Helm et al., 2014). A specifically designed filter is applied to eliminate outliers in the dataset before utilizing the Advanced Kriging method (a form of Ordinary Kriging) to derive a 200 m resolution Digital Elevation Model (DEM) of the entire BBGS surface (Trantow & Herzfeld, 2016). The influence of CryoSat-2 data processing techniques on elevation analysis and numerical modeling results is given in Trantow et al. (2020).

Quiescent experiments presented in this paper are initialized using a DEM derived from aggregated CryoSat-2 TFMRA-swath data from May 2016 to October 2016 (Summer 2016), which corresponds to the initial quiescent phase geometry after the most recent surge. Initial topography for the surge phase experiments are given by the final state of the quiescent simulation. Note that for all experiments in this paper, the FEM grid-resolution is set to 400 m element lengths, which is identical to the resolution for simulations in Trantow and Herzfeld (2018).

3.2.2 Ice/Bed Boundary

The ice-bed boundary condition specifies a friction, or sliding, law that specifies the relationship between basal shear stress and basal velocities and is an important aspect of modeling surge behavior (B. Kamb, 1970; Clarke et al., 1984; W. B. Kamb, 1987). In this section, we cover the both the linear friction law used in modeling the quiescent phase and spatiotemporally evolving law for the surge phase. The surge-phase friction law is an extension of the linear friction law and is modeled to represent the evolution of a surge wave, or "surge-front", that propagates down-glacier during the surge along the central flowline of the glacier.

As mentioned previously, we do not consider bed composition in our simulations (hard vs. soft bed representation) and instead simply model the effect of changing friction at the ice-bed interface. Following Harrison and Post (2003), we use the term "basal motion" to represent the various processes under the ice that result in non-zero basal velocities. Basal motion accounts for nearly all the dynamics during as surge with internal deformation contributing very little to the observed ice-velocities (Cuffey & Paterson, 2010). Even in the quiescent phase of the BBGS, significant basal motion is required to capture the observed velocities throughout most of quiescence (Trantow, 2020).

We estimate the unknown basal friction law parameters through model-data comparisons of crevasses and surface velocities as described for the early-2011 surge phase in (Trantow & Herzfeld, 2018) and for the quiescent phase in (Trantow, 2020). By estimating these parameters using observations, we essentially bypass the need to explicitly model the basal water pressure responsible for the changing basal motion. Some friction laws allow one to infer the basal water pressure after estimating the unknown parameters (see Jay-Allemand et al. (2011b)). A lack of hydrological observations for the BBGS makes these inferences difficult, however we attempt to describe basal conditions in relation to water storage and drainage efficiency based on the modeled mass redistribution and inferred hydropotential (see Section 3.3).

We begin by introducing aspects common to both basal friction representations. For each, we assume ice flow does not penetrate the basal boundary, that is, there is no normal component to ice velocity at the base

$$\boldsymbol{u} \cdot \boldsymbol{n_b} = 0 \tag{8}$$

where $\boldsymbol{n_b}$ is the unit surface normal vector pointing outward to the bedrock surface (Gagliardini et al., 2013).

The input basal bedrock topography, common to all our BBGS simulations, is derived from ice-penetrating radar measurements provided by the Warm-Ice Sounding Explorer (WISE) acquired during a 2012 campaign to the BBGS by NASA's Jet Propulsion Laboratory (Rignot et al., 2013). Derivation of bedrock topography DEMs of the BBGS is described in Trantow and Herzfeld (2018) and in Chapter 4.1 of Trantow (2020).

3.2.2.1 Linear Friction Law for the Quiescent Phase

Basal motion in the direction tangent to the basal surface normal takes place throughout the entire BBGS system during most of the surge cycle, aside from a short (∼1 year) time period immediately after the surge ceases and basal water pressures are fully relieved, when observed ice velocities in Lower and Central Bering Glacier can be fully captured using a no-slip boundary condition (Trantow, 2020). Experimentation in Trantow (2020) and Trantow (2014) show mean basal motion during quiescent flow, throughout the entire glacier system, is approximated using a linear sliding law

$$\sigma_{nt_i} = \beta u_{t_i}, \quad for\ i = 1, 2, \tag{9}$$

which relates the basal shear stresses, σ_{nt_i}, to the basal velocities, u_{t_i}, through the linear friction coefficient β. A constant and uniform value of $\beta = 10^{-4}\ \frac{MPa \cdot a}{m}$ is used for quiescent flow as informed by velocity observations during quiescence (Trantow, 2014, 2020). The uniform prescription of β across the entire glacier system serves as a first-order approximation of the basal conditions during quiescence. We expect the friction coefficient to depend on effective pressure, $\beta = \beta(N)$, which would not be uniform throughout the glacier. While the results of our first-order quiescent simulation match observations quite well, we suggest ways to improve the spatiotemporal distribution of β based on model results and observed quiescent velocities in Section 4.4.

3.2.2.2 Spatiotemporal Friction Law for the Surge Phase

During a surge, the linear friction representation adequately captures the spatiotemporally local behaviors of ice flow as shown in (Trantow & Herzfeld, 2018). That is, the linear sliding law accurately captures observed ice dynamics for an ∼20 km longitudinal segment of the glacier for ∼3 months. This spatiotemporal-segment of ice dynamics corresponds to the ice that is actively surging during the surge-phase evolution. We use this information, along with additional velocity observations, to derive a spatiotemporally evolving basal friction law for the surge phase that utilizes the linear relationship between basal shear stress and basal velocities. This amounts to finding a distribution for the linear friction coefficient that evolves in space and time, $\beta = \beta(x, t)$. Physically, the law models the propagation of a surge front, which acts as an activation-wave that changes basal conditions, a la (Fowler, 1987). We use observations of a propagating front prior to and during the latest BBGS surge in 2008-2013 to estimate parameters in the new spatiotemporally-varying friction law that follows (Turrin et al., 2013; Trantow, 2020).

These parameters include the surge-wave propagation speed, u_{sf}, the surge-wave initiation location x_{init}, a minimum linear friction coefficient, β_{min}, corresponding to the peak surge velocity, and a linear friction coefficient corresponding to unactivated ice, β_q, equivalent to the quiescent phase value. These parameters help define a spatial distribution of basal linear friction values that evolves in time throughout the surge phase. The surge-phase friction law is specified along a 1D central flowline, whose distance from the upper glacier boundary is given by x (see Figure 3). Values for β throughout the 2D ice-bed interface are given by the closest along-flowline point. A more complex representation is needed to capture the transverse variations in glacier flow that have been observed in Central Bering Glacier during a surge, which manifest as branches in the flow regime divided by the deep central glacier trough (U. C. Herzfeld et al., 2013; Trantow, 2020).

A formula for the propagation speed of the surge front, u_{sf}, is given by Fowler (1987) in terms of heights and velocities for each edge of the surge front. In our implementation of the surge wave here however, we assign a fixed propagation speed of 50 m/day which is on par with the observed propagation speed of the kinematic wave from 2008-2010 through Bering's trunk an ịnto the lobe area (Turrin et al., 2013). Characteristics of the glacier at the end of quiescence will inform a choice of a surge initiation location along-flowline x_{init} (see Section 5.1).

With the surge-wave propagation speed and the initiation location we can define the bounds an activation zone of actively surging ice, given by the leading and trailing edge locations, at any time during the surge phase: $x_{active}(t) = x \in [x_{trail}(t), x_{lead}(t)]$. The location of the leading edge of the surge front is given by:

$$x_{lead} = x_{init} + u_{sf} \cdot t \tag{10}$$

where t is simulation time in years. Based on velocity observations of the surge front propagation in Turrin et al. (2013), we set the trailing edge location equal to the initiation location since velocities appear to be elevated in Upper Bering Glacier throughout the surge in 2008 through 2010. Therefore,

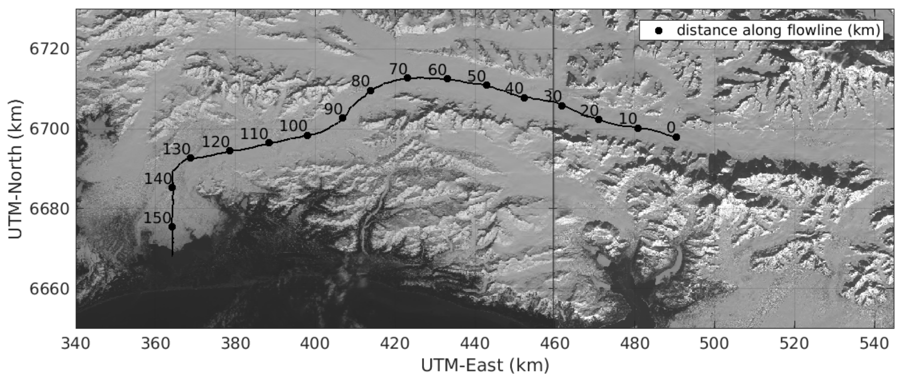

Figure 3. Flowline along the BBGS with 0 km corresponding to the uppermost point the system in the Bagley Ice Field. The Bagley Ice Field stretches from km-0 to the Bering-Bagley Junction (BBJ) at km-80. Upper Bering roughly corresponds to segment of Bering Glacier from km-80 to km-100, Central Bering from km-100 to km-130 and Lower Bering (or the Bering Lobe) from km-130 to km-155 at the terminus. Most of the interesting surge dynamics occur in Bering's main "trunk" which stretches from km-80 to km-135.

$$x_{trail} = x_{init} \tag{11}$$

Ice up-glacier and down-glacier of the activation zone is considered "unactivated ice" and is assigned the quiescent phase value for the linear friction coefficient, β_q.

The final part of defining of basal friction coefficient during the surge-phase is given by the distribution of the β values within the activation zone. Observed surface speeds are largest near the leading edge and generally decrease as you move up-glacier (W. Kamb et al., 1985; Fowler, 1987; Raymond et al., 1987). By estimating linear friction values from observed surface velocity data from the 1982-1983 surge of Variegated Glacier, Jay-Allemand et al. (2011b) found the β distribution within the activation zone resembled a normal curve whose peak was near the leading edge. At some times during the surge, the estimated β distribution contained an additional peak up-glacier of the leading edge, which Raymond et al. (1987) suggest is due to irregularities in the bedrock topography. Based on the distribution of model-data discrepancy in surge velocities in lower Bering in Trantow and Herzfeld (2018), we decide to use a simple linear distribution of β within the activation zone. We assign the minimum friction coefficient at the leading edge of the surge front, β_{min}, and have β linearly increase throughout the activation zone until its end at the trailing edge where the friction coefficient is set to its quiescent value, β_q. Given the description here, the linear friction coefficient along the entire flowline axis (x) is defined mathematically as:

$$\beta(x,t) = \begin{cases} \beta_{min} + (\beta_q - \beta_{min}) \frac{x_{lead}(t) - x}{x_{lead}(t) - x_{trail}}, & if \quad x_{trail} \leq x \leq x_{lead} \\ \beta_q, & otherwise \end{cases} \tag{12}$$

for $t > 0$, with $t = 0$ corresponding to the time of surge initiation. The simulations in this paper use a quiescent friction coefficient of $\beta_q = 10^{-4}\ \frac{MPa \cdot a}{m}$ based on results from Trantow (2014). The surge-front basal friction coefficient value, β_{min}, is set to $\beta_{min} = 10^{-5}\ \frac{MPa \cdot a}{m}$, which comes from a result of optimizing the linear basal friction coefficient for the surge front in early-2011(Trantow & Herzfeld, 2018). The linear transition between the two values within the activation zone describes an approximation to the observed surge progression during the latest surge, as mentioned previously. A diagram of the basal friction coefficient distribution within the activation zone is given in Figure 4.

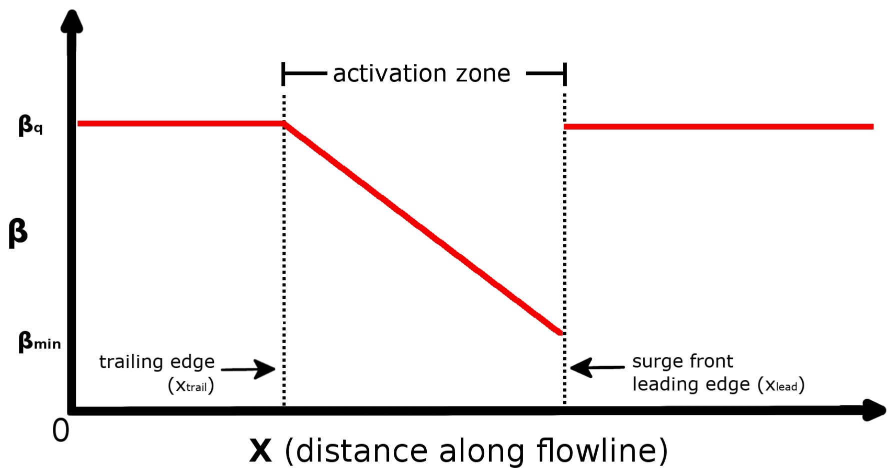

Figure 4. Linear basal friction coefficient distribution during the surge phase. Basal friction coefficient, β, versus along-flowline distance, x, where $x = 0$ is the uppermost location in the Bagley Ice Field.

3.2.3 Lateral Boundary

The material similarity of the glacier's base and margins leads to a prescription of the linear friction law at the lateral boundary as well. However, the friction coefficient is larger, reflecting more friction, as there is significantly less water lubrication along the sides of the glacier compared to the base. Experimentation in Trantow (2014) suggests the lateral friction coefficient, $\beta = \beta_{lat}$, is 5 times larger than the nearest basal sliding coefficient based on observed velocities and shear behavior near the margins.

We treat the lateral margins uniformly throughout the entire glacier perimeter by assuming a rigid, mountainous boundary (with or without till). This representation, however, does not hold for behavior at the glacier terminus. Calving at Bering Glacier's terminus is a complicated process somewhat unique among surge-type glaciers in that it calves into a series of proglacial lakes, the largest of which is Vitus Lake, rather than the ocean (Lingle et al., 1993). Throughout most of the surge cycle, the terminus is grounded at the lake bed being held down by the tensile strength of the ice. Unbalanced hydrostatic pressure acting on the glacier bottom pushes upwards at the glacier front resulting in a bending moment. The bending moment causes a fracture, likely at the point of maximum moment occurring at the glacier base, eventually leading to calving events. Since Bering Glacier is grounded below hydrostatic equilibrium, the icebergs pop up once calved, and float at a higher elevation than the grounded ice at the terminus. The calving mechanism occurring during the surge phase is unknown but likely takes the form of an active calving cliff (Lingle et al., 1993).

We do not model Bering's complicated and changing calving process in this paper and instead treat mass loss from the system due to calving in the following manner. First, we extend the glacier model domain by several kilometers (2-5 km) at the glacier terminus assigning it the minimum ice thickness of 1 meter. The assumed true glacier terminus is derived from satellite imagery in 2016, marked by a solid black line in Figure 6, while the extended model boundary is given by observations of the terminus at its maximal extent after the most recent surge (Trantow, 2020). We treat all ice-mass that crosses into this extended region as ice lost to the system via calving. During the surge, the ice movement into this region may be seen as an approximate representation of terminus extension, but without a retarding force due to lake water. The latest surge extended Bering's terminus 2-4 km (Turrin et al., 2013), therefore our region of minimum ice thickness is large enough to account for this phenomenon.

3.3 Hydropotential as a Proxy for Subglacial Drainage

Observations of subglacial hydrological systems are sparse, difficult to interpret and often do not provide the necessary information required to constrain parameters in a subglacial drainage model (Brinkerhoff et al., 2016; de Fleurian et al., 2018). Moreover, there are very few applications of subglacial hydrological models to real topographies and forcings due to the modeling difficulties (de Fleurian et al., 2018). The absence of any comprehensive hydrological measurements for the BBGS, combined with the difficulty of applying a sophisticated subglacial hydrological model to a large and complex glacier system, we choose to use a calculation of hydraulic potential (hydropotential) and its gradient to infer characteristics of the subglacial hydrological system throughout the surge cycle. We investigate the hydraulic gradient along the one-dimensional flowline whose coordinates are given x (see Fig. 3).

In this study we use the Shreve Potential (Equation 14) (Shreve, 1972) to estimate hydropotential and investigate evolution of glacial hydrologic characteristics throughout the surge cycle. More specifically, the gradient of hydropotential (hydraulic gradient) is used as a steady-state proxy for water flow. Water is estimated to flow from areas of high to low hydropotential in the direction of the (negative) hydraulic gradient. This approach has had success in predicting actual subglacial hydraulic characteristics (e.g., Sharp et al. (1993); Chu et al. (2016)). However, the calculation and subsequent analysis of the Shreve Potential requires several assumptions that are perhaps unrealistic for actual glaciers, which we discuss here as we introduce the mathematics.

Given a certain glacier geometry, the hydropotential calculation is calculated by knowing the ice thickness and water pressure at some point within the glacier. The expression for hydropotential Φ at the bed is given by,

$$\Phi = \rho_w g z_b + p_w \tag{13}$$

where ρ_w is the density of water, z_b the elevation of the bedrock and $p_w = \rho_i g h - N$ the water pressure with ρ_i representing ice density and N effective pressure. Here we arrive at our first major assumption which assumes the effective pressure is zero everywhere, that is, the ice overburden pressure is approximately equal to the water pressure ($\rho_i g h \approx p_w$). This is only realistic if water completely fills the subglacial (or englacial) drainage conduit, and its enlargement rate is assumed to be the same at every location. During the surge, the rapid basal motion, due to increased basal water, implies an effective pressure at, or at least near, zero. Moreover, as shown in the flow-dynamic experiments in Trantow (2014), the quiescent phase velocities cannot be accurately captured without accounting for basal motion which also implies a very low effective pressure, making this assumption reasonable for the BBGS throughout most of its surge cycle as far as predicting drainage paths goes.

With the $N = 0$ assumption, hydropotential can be calculated by,

$$\Phi = [\rho_i z_s + (\rho_w - \rho_i) z_b] g = \rho_i g h + \rho_w g z_b, \tag{14}$$

where $h = z_s - z_b$ is the height of the glacier. In this form, we see the hydropotential is simply the combination of ice overburden pressure and the elevation (or topographic) potential.

Aside from the zero effective pressure assumption, this formulation also assumes: (1) the glacier ice and subglacial till have an intrinsic permeability that is homogenous and isotropic, and (2) the recharge of water to the glacier bed is spatiotemporally uniform (Gulley et al., 2009, 2012). The spatiotemporal heterogeneity of both subglacial water recharge, i.e., water entering the subglacial drainage system, and hydraulic conductivity at the glacier bed have both been identified by Gulley et al. (2012) to be important components of estimating hydropotential, and they are not accounted for in the formulation of Equation 14. However, given our available data sets and the usefulness the Shreve potential approach to estimate subglacial drainage characteristics in some previous studies (Sharp et al., 1993; Chu et al., 2016), we proceed to estimate hydropotential using Equation 14 keeping in mind its assumptions and limitations.

3.4 Surface Mass Balance Forcing

Annual accumulation and ablation estimations for the BBGS are given by Tangborn (2013) as a function of ice-surface elevation while Larsen et al. (2015) provide SMB rates for glaciers across Alaska, including the BBGS. Tangborn (2013) employs a PTAA (precipitation-temperature-area-altitude) model, using daily precipitation and temperature observations from nearby weather stations to derive historical net ablation and accumulation balances with respect to ice-surface altitude from 1951-2011. More recently, Larsen et al. (2015) used airborne altimetry to estimate regional mass balances for Alaskan mountain glaciers. The rates given by Tangborn (2013) estimate much higher melt-rates for the BBGS which are at odds with the more recent and comprehensive measurements by Larsen et al. (2015). We therefore enforce accumulation and ablation rates whose magnitudes better reflect those measured by Larsen et al. (2015), but still employ the quasi-linear relationship of SMB rates with respect to ice-surface altitude derived by Tangborn (2013).

Figure 5 shows the linear relation between our enforced SMB and ice-surface elevation. A histogram describing the distribution of ice-surface elevation at each model surface-node throughout the BBGS is also shown in the same plot. The slope of the line is derived from a linear approximation, fit in a least-squares sense, of the mean net mass balance for the BBGS from 1951-2011 converted to meters per year of ice from the original mean-water-equivalent per year in Tangborn (2013). This conversion requires an assumption of constant ice density which is set at 917 kg/m^3 (ice density for the 0°C isothermal assumption). The y-intercept is adjusted so that the function spans the observed range given by Larsen et al. (2015). SMB forcing is applied uniformly in a temporal sense and does not account for seasonal variability in accumulation or ablation.

The equation for enforced annual mean-SMB (in terms of meters of ice gain/loss), smb_{mean}, is given by glacier surface elevation z:

$$smb_{mean} = \Big(0.0015 \cdot z - 2\Big)/0.917 \tag{15}$$

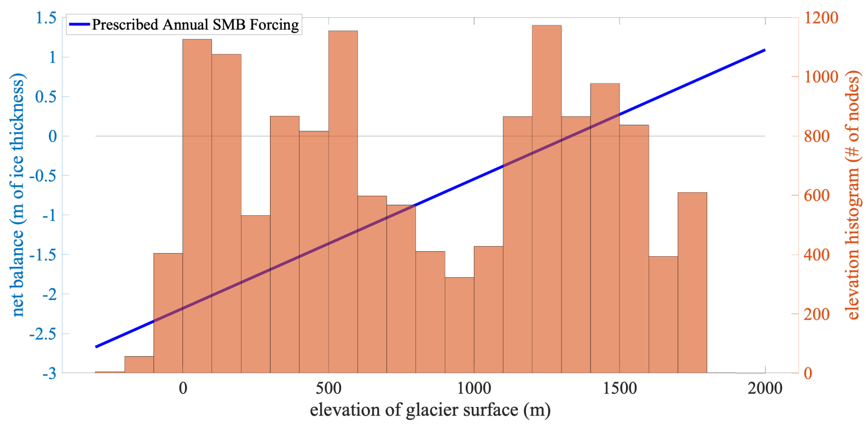

Figure 5. Annual net surface mass balance estimates for Bering Glacier as a function of elevation derived from Larsen et al. (2015) and Tangborn (2013). The blue line gives the linear approximation of relationship between glacier surface elevation and surface mass balance based on Tangborn (2013) while the magnitude of surface mass balance is based on Larsen et al. (2015). The histogram shows the distribution of model surface-nodes at a given elevation throughout the BBGS at the beginning of quiescent phase experiment (Summer 2016 geometry).

4 The Quiescent Phase

Prognostic simulations of the entire quiescent phase help identify how mass is redistributed in the BBGS over the course of normal flow, which leads to conditions favorable for surging. After providing some model specifics for the quiescent simulation, we analyze the mass redistribution results and estimate mass loss over 20-years of quiescent flow (Section 4.1). Next we infer changes in the basal hydrological system caused by the mass redistribution through calculation of the subglacial and englacial hydraulic gradients (Section 4.2). We then identify reservoir areas and associated subglacial topography characteristics that are responsible for the observed changes in Section 4.3. Finally, we compare simulated and observed velocity during quiescence and propose a way to increase complexity of the quiescent phase friction law to better match observations in Section 4.4.

We simulate quiescent flow for 20 years using 10-day time increments (730 total time steps), which corresponds to the approximate length of the observed BBGS quiescent phases since 1900 (B. F. Molnia & Post, 2010). While the most recent quiescent phase, beginning in 1996, lasted only 12-15 years, the results in this section remain applicable as changes during quiescent flow are gradual and evolve monotonically. The magnitude of changes expected during the last full quiescent phase however, might not be as dramatic as at given by the 20-year results given in this section.

4.1 Elevation Change and Mass Loss

Figure 6(a) shows quiescent elevation change by differencing the initial surface elevation with the surface elevation after 20 years of evolution. The initial ice surface is taken as the glacier surface after 50 time steps of free evolution in order to reduce any elevation-change signals arising from errors in the input surface DEM (Trantow et al., 2020).

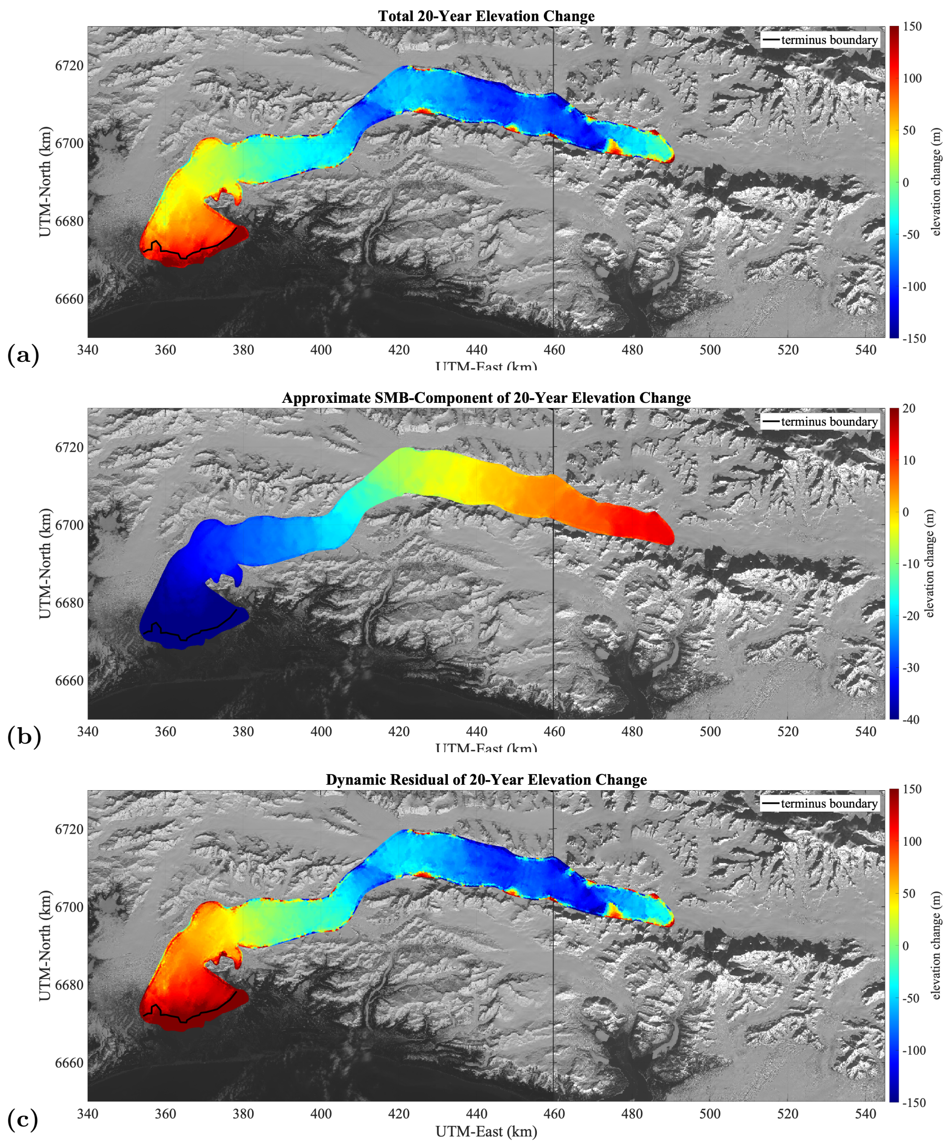

Figure 6. Elevation change results from 20-year quiescent simulation of the BBGS. (a) Total elevation change in meters. (b) Approximate SMB component of elevation change. (c) Approximate dynamic component of elevation change. The black line marks the assumed glacier terminus, derived from the observed 2016 boundary, and is treated as a flux gate to estimate calving.

Figure 6(b) shows the approximate contribution of SMB forcing on the overall quiescent elevation-change signal. The approximation is calculated by applying the SMB rate to the initial topography aggregated for 20 years (the true SMB signal changes at each time step due to a redistribution of ice-surface elevation). With our enforced accumulation/ablation pattern, based on observations in the current realm of climatic warming, it is not surprising that the overall glacier system loses mass. We see accumulation up to 20 m throughout most of the Bagley Ice Field with significant melt rates throughout Bering Glacier and the lower Bagley exceeding 30 meters near Bering's terminus. These rates lead to a total estimated mass loss signal of 25.21 km^3 from SMB over the 20-year simulation (1.363 km^3 per year).

Subtracting the SMB signal from the total simulated elevation-change we receive the dynamic-residual, i.e., the elevation change signal from the dynamics of the glacier (Figure 6(c)). Clearly, the total elevation-change signal is dominated by the dynamics of the glacier which is expected for the relatively fast-moving temperate glaciers of southeast Alaska. Ice loss due to dynamics comes in the form of calving which we estimate as mass passing past the flux-gate marking the initial terminus (black line in Figure 6(c)) and into the extended region at the front of the glacier (see Section 3.2.3). Over the course of the 20 year quiescent phase, we estimate 12.88 km^3 of mass loss due to calving in the BBGS (0.644 km^3 per year). Thus, the combined mass loss is approximately 38.09 km^3 for 20 years (1.90 km^3 per year) with SMB contributing to 2/3 of the signal and mass loss due to dynamics (calving) contributing to 1/3.

4.2 Hydropotential Analysis

We use hydropotential to infer characteristics of the subglacial drainage system that result from changing geometries, as described in Section 3.3, which is an important aspect in understanding surge evolution. Maps of hydropotential provide estimates for the path that water takes through the ice-bed interface as it drains to the glacier terminus, flowing down the hydraulic gradient from high to low (hydro)potential.

The basal hydropotential depends on local ice thickness and can therefore deviate from the topographic gradient of the bedrock, that is, the accumulation of ice in reservoir areas during quiescence changes the basal hydraulic gradient. In general, the steeper the surface slope, the less the glacial drainage flows along the local bed topography (Shreve, 1972). Therefore, we expect the glacier steepening near the reservoir areas to divert the flow of water at the base from its early-quiescent path.

Figure 7 gives a full spatial map of the basal hydropotential of the BBGS in year-1 and year-20 of the quiescent simulation. Colored contours are given at 0.2 MPa intervals while black labeled contours are given at 1.6 MPa intervals. The general direction in which water flows will be perpendicular to the equipotentials of the hydropotential. Subglacial water storage occurs in closed areas of lower hydropotential (hydropotential wells), similar to ordinary lakes forming in closed areas of lower elevation (Shreve, 1972).

These maps indicate that the efficiency of the hydraulic drainage throughout Bering Glacier's trunk, given by the amount of contours per distance along the flowline, is much lower in year-20. The 1.6 MPa black reference lines are given in the figure to help highlight this change. Moreover, we see the development of potential wells throughout Bering Glacier as indicated by the arrows in Figure 7(b).

To better visualize and quantify these subglacial drainage changes in Bering Glacier's trunk, we created along-flowline plots of the hydropotential and hydropotential gradient by averaging the values across the glacier width. Figure 3 gives a reference to the along-flowline distance starting at the uppermost accumulation zone near the Eastern Bagley Ice Field's confluence with Columbus Glacier, and ending ∼157 km down glacier at Bering's terminus. Note however, that labeling this the flowline is somewhat misleading as several flow regimes exist and multiple subglacial troughs divide the flow across the glacier width, especially near the lobe area past the 125 km mark (B. F. Molnia & Post, 2010; Trantow, 2020).

Figure 8(a) shows the mean along-flowline elevation (dashed) and hydropotential (solid) at the beginning (red) and end (blue) of the quiescent experiment over the trunk of Bering Glacier (km-80 to km-135). Note that it is the *difference* in hydropotential, across some fixed distance, that is the salient measure of hydraulic flow efficiency rather than the magnitude of hydropotential at some location. We therefore analyze the difference in hydropotential across Bering Glacier's trunk which has decreased by 16.6%

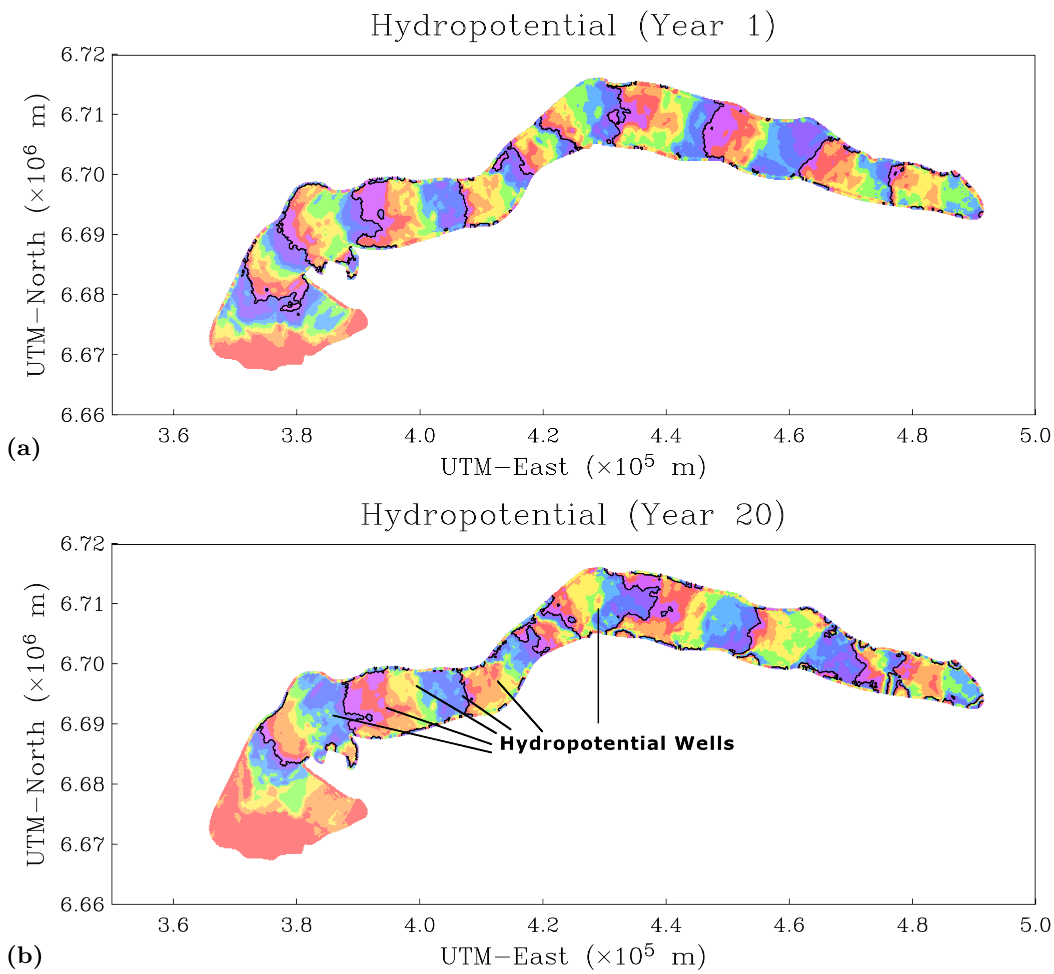

Figure 7. Modeled basal hydropotential for at the beginning and end of the 20-year quiescent phase simulation of the BBGS. Colored contours are given at 0.2 MPa intervals while black-lined contours are given at 1.6 MPa intervals. (a) Basal hydropotential for at the beginning of the quiescent phase in year 1. (b) Basal hydropotential at the end of a 20-year quiescent phase. The black lines indicate notable hydropotential-wells that have grown or developed over the course of 20-years of quiescent flow.

over the course of quiescence. Even without considering the existence of hydropotential wells, this result suggests that Bering Glacier's trunk is draining basal water less efficiently down-glacier, with more transverse drainage paths, assuming a fixed water inflow rate.

Figure 8(b) shows the mean along-flowline hydraulic gradient of Bering Glacier's trunk over the course of quiescence, indicating drainage rates down-glacier and locations where Bering Glacier is storing basal water as indicated by a positive hydraulic gradient. Clearly, the amount of water being stored at the end of quiescence (blue solid line above 0, shaded for clarity) has increased significantly from the beginning of quiescence (red solid line). The amount of water stored in the hydropotential wells, as estimated by the area of each line above zero, has increase by 246% over the course of quiescence. These well-areas, and other areas where the hydraulic gradient is less than zero along the flowline, correspond to the surge "trigger zones" identified in Robin and Weertman

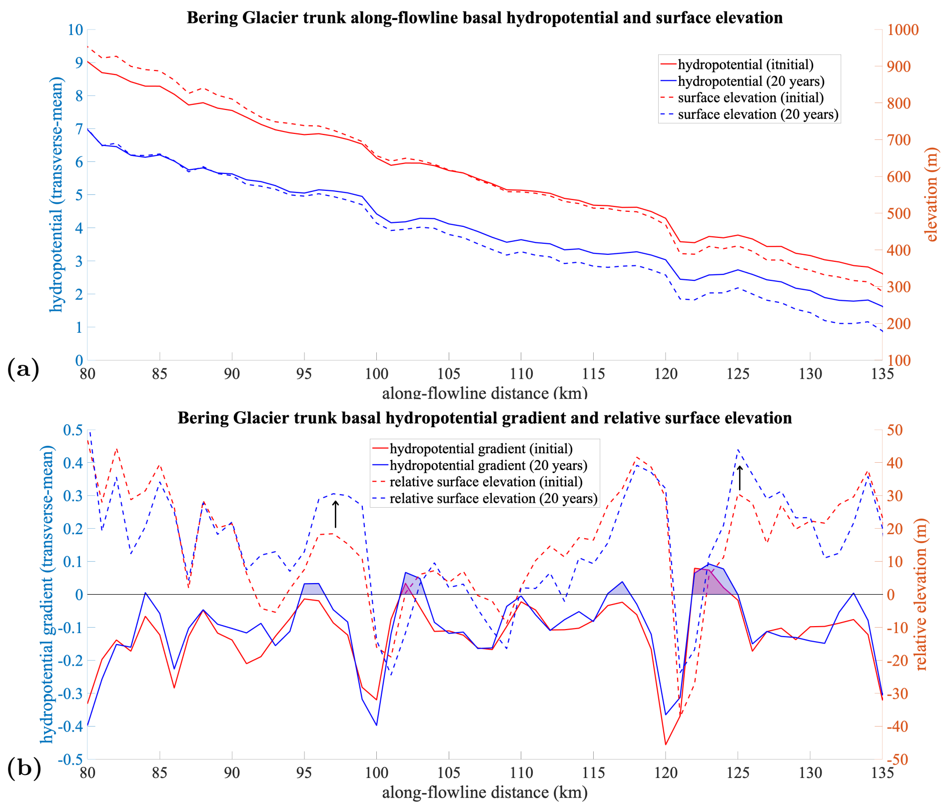

Figure 8. Change across the Bering Glacier trunk with regards to hydropotential and surface elevation over the course of the modeled quiescent phase. Red lines reflect the glacier state at the beginning of quiescence while blue lines reflect the end of quiescence state. (a) Hydropotential (solid lines) and surface elevation (dashed lines). (b) Hydropotential gradient (sold lines) and relative surface elevation (dashed lines). Relative surface elevation is calculated by removing the mean slope of surface elevation. Shaded areas reflect locations where the hydropotential gradient is above zero implying water flowing up-glacier, i.e., subglacial water storage. Black arrows indicate growing surface bulges.

(1973) where basal water is "dammed" increasing stored water in the up-glacier zones where the hydraulic gradient is near-zero, which corresponds to the "collection areas".

The dashed lines in Figure 8(b) show the relative elevation initially (red) and after 20-years of quiescent flow (blue). Relative elevation is found by subtracting the mean slope from the elevation profiles in Figure 8(a) and indicates where reservoir areas, or surface bulges, are forming. The black arrows around km-97 and km-123 indicate building reservoir areas, while the high relative-elevation area around km-118 retains a fixed magnitude throughout the quiescent phase while steepening on it's up-glacier-side. The enlarging reservoir areas and steepening of local geometry lead to increased stored water in the areas 2-4 km up-glacier of these bulges. We also identify an area of stored water around km-102 without a large corresponding surface bulge, however, the relative surface slope in this area is steepening.

4.3 Reservoir Areas and Bedrock Topography

The locations of the reservoir areas, along with the basal water storage areas, are attributed to the characteristics of Bering Glacier's bedrock topography, shown in Figure 9(a), whose shape is influenced by the local faults (Koehler & Carver, 2018; Trantow, 2020). In particular, it is the extension of the surrounding mountain ridges underneath the glacier, termed "subglacial ridges", that are responsible for damming ice at these locations. Black arrows in Figure 9 point out some of the significant subglacial ridges. Directly up-glacier of these ridges are local deepenings in the basal topography where water collects. Ice-mass build-up in front of these deepenings, caused by the subglacial ridges, slows the down-glacier drainage resulting in increased water retention in this area as shown in Figure 8(b).

The 3 reservoir areas we have identified through our quiescent phase simulation are circled in red in Figure 9(a) and the four areas of subglacial water storage are circled in dark purple. These areas are possible locations where surge initiation (or re-initiation) occurs, likely at the down-glacier edge of the reservoir areas where ice-surface geometry is steepest. The reservoir area centered at km-97 with a leading edge at km-100, termed RA-97, is identified by Burgess et al. (2013) to be the reservoir area for the initial surge phase in early-2008, which, after mass transfer to the receiving areas, likely caused the observed rift in the former receiving area (U. Herzfeld, 1998; U. C. Herzfeld et al., 2013; Trantow, 2020). D. R. Fatland and Lingle (2002) hypothesize that RA-97 is the reservoir area for the 1993-1995 surge of Bering Glacier. RA-97 is formed by two transverse pairs of subglacial ridges just up-glacier of Ovtsyn Glacier on the north margin and just down-glacier of Kuleska Glacier on the south margin. Ice-mass accumulates behind the ridges, filling the deep bedrock depression, giving the thickest ice in all of Bering Glacier.

The reservoir area centered at km-124 with a leading edge at km-126, termed RA-124, is identified as the reservoir area in 2010/2011 by U. C. Herzfeld et al. (2013) for the major surge phase occurring in early 2011, who measured a prominent surface lowering at this location of over 50 m in the summer of 2011 indicating a bulge collapse after the surge had been progressing for several months. Down-glacier of RA-124 in the Bering lobe is an area of complex topography where the deep trough running through Bering's trunk splits into two major branches, which we term the Tashalish Trough in the west and the Grindle Trough in the east, with even more subglacial troughs appearing further down-glacier in the lobe area. The Khitrov and Grindle Hills on the north and south side of the glacier respectively, produce large subglacial ridges that serve to accumulate ice before it crosses the Khitrov-Grindle line by flowing down a particularly steep section of bedrock into the lobe area. This steep slope, identified along the Grindle Corner in aerial imagery by a series of ice falls (U. C. Herzfeld et al., 2013; Trantow & Herzfeld, 2018), explains why the surge wave, as measured by Turrin et al. (2013), speeds-up once it reaches this area.

Subglacial ridges that continue from nearby mountain ridges are also frequent in the Bagley Ice Field, as seen in Figure 9(b), causing ice-mass build-ups directly up-glacier (specifically near km-64, km-41, km-31, km-23, km-12 and km-3). Their existence in the BIF is evident from the topographically induced en-échelon crevasses (Figure 2(f)) (U. C. Herzfeld & Mayer, 1997; U. C. Herzfeld et al., 2013).

The Bagley Ice Field does not experience a full-scale surge of its own due to a lack of melt-water throughout the ice field. As seen in our SMB prescription (Figures 5 and 6(b)), along with Larsen et al. (2015), most of the Bagley Ice Field lies in the accumulation zone of the glacier system and experiences minimal surface melt throughout the year. The lower part of the Bagley Ice Field does experience significant melt with a net-negative SMB balance down-glacier of km-60. The reservoir area at km-64 (RA-64) coincides in location with a small acceleration event (mini-surge) identified by Burgess et al. (2013) that occurred in the Bagley Ice Field during quiescence in 2003. Based on the local basal topography, the released basal water during the mini-surge event would divert northwest through Tana Glacier, quickly exiting the subglacial drainage system, and little basal water would be expected to flow across the BBJ into Bering Glacier. Tana Glacier is significantly shorter and thinner than Bering Glacier, with shorter water drainage

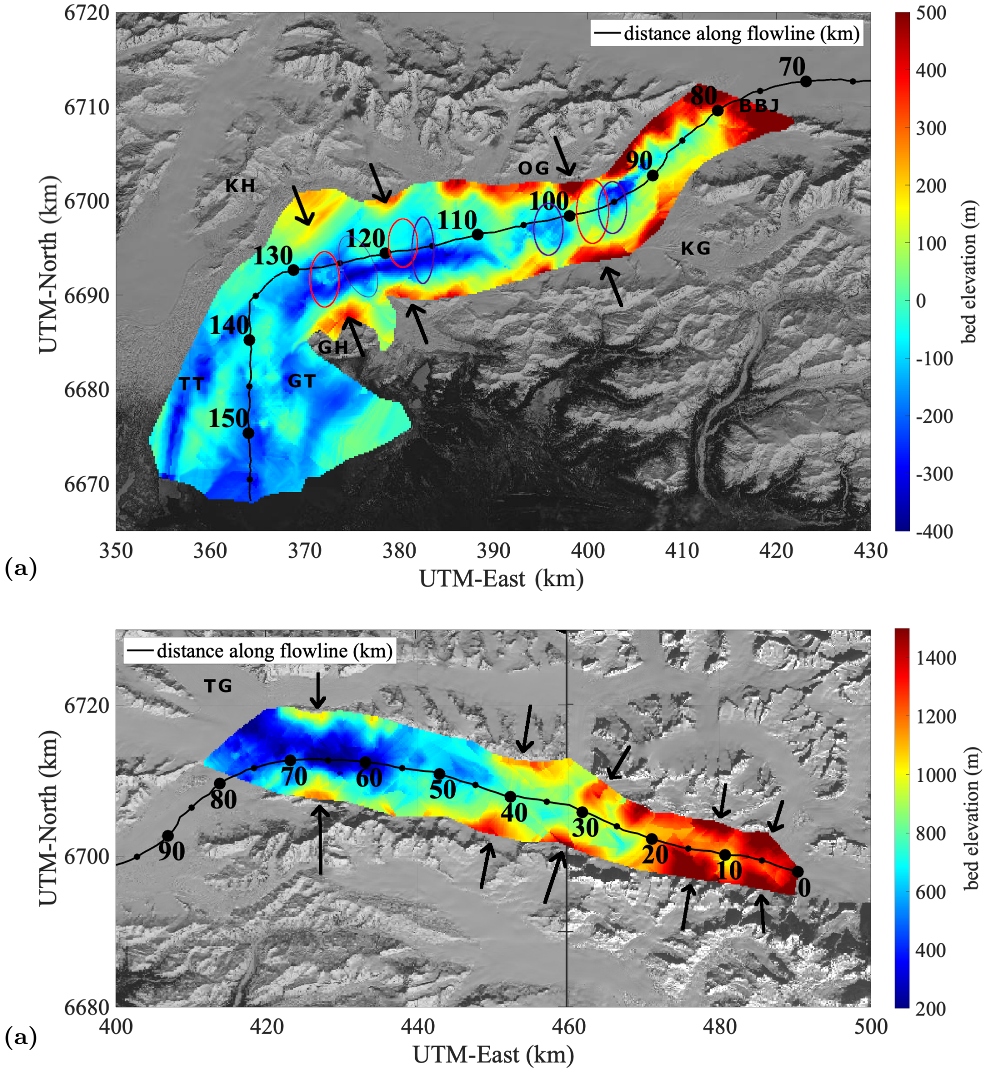

Figure 9. Locations of estimated reservoir areas and water storage over bedrock topography for Bering Glacier and the Bagley Ice Field. The along-flowline distance is given by the black line (km) while black arrows indicate subglacial features that contribute to the formation of the reservoir areas. a) Bering Glacier bedrock topography. Possible reservoir areas are circled in red and water storage areas are circled in dark purple. (b) Bagley Ice Field bedrock topography with notable subglacial ridges indicated by arrows. BBJ – Bering-Bagley junction, TG – Tana Glacier, KG – Kuleska Glacier, OG – Ovtsyn Glacier, TT – Tashalish Trough, GT – Grindle Trough, KH – Khitrov Hills, GH – Grindle Hills.

passageways, and can evolve more readily to accommodate up-glacier changes in mass and water flux. Tana Glacier is not observed to surge (Burgess et al., 2013), and thus mass imbalances and water retainment likely do not occur on the scale that they do in Bering Glacier.

Lingle and Fatland (2003) describe velocities in the BIF during the 1993-1995 BBGS surge using SAR interferometry and found a large "bullseye" at the location of RA-64. The bulls-eye corresponds to englacial water build-up that had caused vertical motion in the glacier during the 1993-1995 BBGS surge. Due to RA-64's location just above the

BBJ, hydraulic changes experienced here may have some affect on Upper Bering Glacier where the surge is thought to initiate.

4.4 Velocity and Friction Law Improvements for the Quiescent Phase

We compare modeled velocity to observed velocity during the quiescent phase in order to (1) check that our modeled velocity is close to observations and (2) use the differences to suggest ways to improve the quiescent phase modeling. Figure 10(a) gives the observed mean annual velocity across the BBGS from 2020-03-08 to 2021-03-03 as derived from Sentinel 1A imagery using the SNAP toolbox (provided for analysis of SAR data by ESA,(Veci et al., 2014)). We see that most of the glacier system moves at a rate less than 0.5 m/day, but there are pockets of accelerated flow throughout that reach up to 5 m/day. These pockets coincide with the areas of water retainment identified in the previous section. This result suggests that the observed acceleration pockets are correlated with local hydraulic drainage inefficiencies leading to low effective pressures. Maps during other years of quiescence show similar patterns (Trantow (2020), Chapter 4.2).

Figure 10(b) gives the modeled velocity near the end of quiescence at the same scale as the observed velocity in (a). Similar to observations, our model predicts that most of the glacier moves slower than 0.5 m/day, with areas of accelerated flow. The areas of accelerated flow however, do not directly coincide with observations. Figure 10(c) shows the observed velocity minus the modeled velocity with a mean difference of -0.21 $\pm$ 0.63 m/day across the BBGS.

Figure 10(d) plots the along-flowline velocity difference (blue) averaged across the glacier width versus the smoothed hydraulic gradient along-flowline (red). The hydraulic gradient is smoothed across a 5 km length to avoid high frequency signals that may result from errors in the basal topography. We find that the hydraulic gradient at locations in Bering Glacier and lower Bagley, i.e. the ablation zone down-glacier of km-65, coincide remarkably well with the difference between observed and modeled velocity. That is, locations where our model over-estimates surface velocity the hydraulic gradient is relatively low and vice versa. A similar relationship holds for the accumulation zone in mid and upper Bagley, but the proportionality constant is different likely owing to the fact that there is less basal water present.

Such a clear relationship between the hydraulic gradient and velocity discrepancies leads us to investigations of a quiescent phase friction law that depends on the gradient of hydropotential, i.e.,

$$\beta = \beta(\nabla\Phi) \tag{16}$$

where β is the linear friction coefficient from Equation 9 and $\nabla\Phi$ is the hydraulic gradient. Here, the easy to calculate hydraulic gradient would be a proxy for the effective pressure, N, which is difficult to measure as it depends of basal water pressure. Such a law for the BBGS quiescent phase could start with a uniform friction coefficient equal to $10^{-4}\ \frac{MPa \cdot a}{m}$ as we do in our simulations here, with adjustments to this value occurring throughout the model run based on the calculated hydropotential. The inclusion of hydropotential calculations would also improve the surge-wave friction law (Equation 12) which is based on the linear friction law used during quiescent simulation. We leave further investigations of this type to later studies and proceed to model the initial surge phase of the BBGS in the next section.

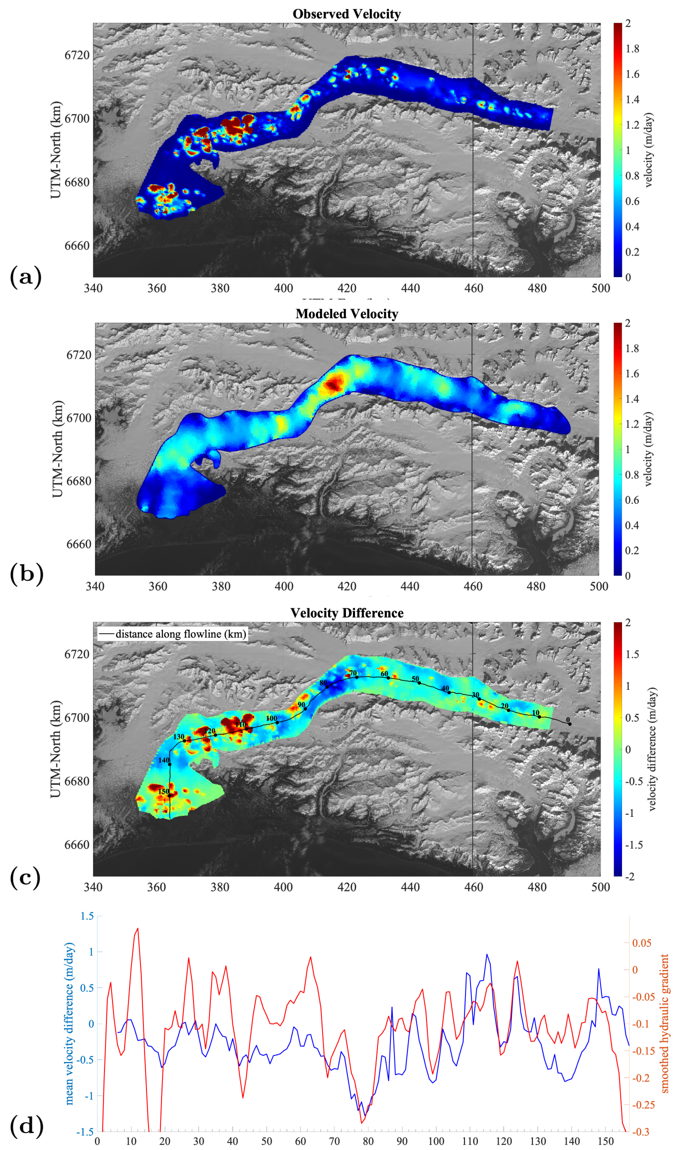

Figure 10. Observed and modeled ice-surface velocity during the BBGS quiescent phase. (a) Observed velocity derived from Sentinel-1 SAR imagery (S1A, 2020-03-08 and 2021-03-03). (b) Modeled velocity near the end of quiescence. (c) Observed-modeled velocity difference with along-flowline distance plotted in black (observed minus modeled). (d) Mean velocity difference (blue) and smooth hydraulic gradient (red) along-flowline.

5 The Surge Phase

As mentioned previously, the model simulates glacier dynamics using a 3D full-stokes representation since we do not wish to impose any stress-related assumptions on the glacier, especially during the surge when rapid deformation of ice occurs in all three spatial dimensions. Our computational resources at the time of analysis however, are limited and therefore we decided to model only the ∼2-year initial surge acceleration as it progresses through the trunk of Bering Glacier (corresponding to the 2008-2010 phase of the most recent surge). A full-Stokes simulation of the full surge phase that includes the second surge phase, most recently occurring in 2011-2013, is calculated more feasibly using high-performance computing which is left for future work. In the mean time, we supplement interpretation of the the second surge phase and the return to quiescence using observed CryoSat-2 Digital Elevation Models and Landsat-derived velocity maps from 2011 and 2013 (Trantow & Herzfeld, 2016).

In this surge phase section, we begin by providing several surge initiation criteria in Section 5.1 based on the results of the quiescent phase experiments which could serve to link quiescent and surge simulations in future experiments. Next, we present the results of our two-year surge-simulation of the BBGS's initial surge phase given by a surge-wave propagating trough Bering Glacier's trunk in Section 5.2. We present results of modeled velocity (Section 5.2.1), basal shear stress (Section 5.2.2), elevation change (Section 5.2.3) and hydropotential (Section 5.2.4) at various time stamps throughout the simulation. Finally, in order to complete our picture of the surge past the initial phase, we use CryoSat-2 observations in Section 5.3 to analyze mass redistribution and hydraulic drainage efficiency during the 2011-2013 phase of the most recent BBGS surge (second surge phase) ending with the transition back to a quiescent state (Section 5.4).

5.1 Surge Initiation

One of the least understood mechanisms of surging is surge-initiation. In this section we investigate our end-of-quiescent results to identify glacier conditions that would initiate a surge. The traditional surge hypothesis states that surges are triggered due to an internal change in the system such as the collapse of an EDS (Meier & Post, 1969; Clarke et al., 1984; Raymond, 1987; Harrison & Post, 2003). Trantow (2020) showed that surge initiation of the last three BBGS surges showed no clear correlation with nearby precipitation and temperature anomalies as measured by the nearby Cordova weather station. We therefore use particulars of the glacier geometry and the basal drainage system, via hydropotential analysis, to derive a surge-initiation criterion as justified in the following.

A changing glacier geometry over quiescence leads to stress conditions that can cause sudden changes in the glacier drainage system (Robin, 1969). An EDS can be destroyed when large overburden pressures from a growing reservoir area overcome the low water pressures experienced by temperate glaciers during the winter season. An IDS then develops up-glacier of the collapse. As melt water input begins to increase in late winter, water pressure increases throughout the IDS which spans the entire width due to restrictive down-glacier drainage (W. Kamb et al., 1985; W. B. Kamb, 1987). If the IDS persists, the rising water pressure will eventually leads to surging, either through a total decoupling of the ice from the hard bed or through dilation of the subglacial sediment (W. B. Kamb, 1987; Truffer et al., 2000; Flowers & Clarke, 2002a, 2002b; Fleurian et al., 2014). Note that an EDS collapse and an IDS formation may occur without resulting in a surge if the EDS can recover before the water pressure reaches a critical level. The recovery time allowed before surging occurs however, becomes shorter with the growing amount of stored water up-glacier of the EDS collapse. That is, lower effective pressures across the glacier width in these areas are achieved quicker this time of year as the quiescence phase matures.

An EDS collapse is likely to occur at locations with steep hydraulic gradients where water is least likely to accumulate and maintain the water pressure for a functioning drainage channel (W. Kamb et al., 1985; W. B. Kamb, 1987). As seen in Figure 8(b), the steepest (and negative) hydraulic gradients are modeled near the leading edge of the reservoir area bulges, particularly at km-100 and km-120. We see that the growing reservoir area at km-97, with a leading edge around km-100, causes a steeper hydraulic gradient to develop near the leading edge while the gradient gets less steep at the km-119 reservoir area where the shape of the leading edge remains relatively constant. The initial surge was observed to trigger near km-97 to km-100 in the latest surge Burgess et al. (2013), and for the purposes of this paper we trigger the surge simulation at this location after the 20 year quiescent evolution.

For future simulations that run over the course of an entire surge cycle, we would adopt a deterministic or probabilistic model to determine when and where the surge would be triggered though this task is made difficult with little to no subglacial or hydrological measurements. For example, a simple deterministic estimation of surge initiation based on our hydropotential results could be made by setting a threshold on the amount of subglacial water storage up-glacier of an increasingly steep hydraulic gradient. Alternatively, instead of a purely deterministic surge initiation criterion, a probabilistic method could be adopted whose density function is based on the hydraulic gradient.

5.2 Surge Simulations

In this section, we present the results from the ≈2-year early-surge simulation applied to the modeled end-of-quiescence geometry using the surge-wave friction law proposed in Section 3.2.2.2. Based on observations of the surge wave during the latest surge by Turrin et al. (2013), we set the surge-wave propagation speed to $u_{sf} = 50$ m/day (18.25 km/year) and as mentioned in the previous section, we set the along-flowline surge initiation location to $x_{init} = 100\ km$, i.e., at the leading edge of RA-97. We use 132 5-day time steps and do not include SMB forcing due to the short length of the experiment. The presented surge experiment models only the surge progressing through the mid to lower Bering Glacier trunk and corresponds to roughly the first two years of the surge (corresponding to ∼2008 through 2010 of the latest BBGS surge).

5.2.1 Velocity

Figure 11 displays the surface velocity at various times during the simulated surge through Bering's trunk. Near the beginning of the simulation, when the surge has only affected a portion of the glacier (from km-100 to km-110), large surface velocities exceeding 1800 m/year (∼5 m/day) are identified. The fastest speeds at this time reach 10.25 m/day which is similar to maximum observed velocities in this area given by Burgess et al. (2013) of 9 m/day. At later time steps, when the surge is progressing down-glacier, velocities subside in this area. When the surge front is moving through the thick ice along km-110 to km-120 (subfigure (c)), modeled ice-surface velocities are noticeably reduced with no areas of the glacier away from the margins exceeding 1000 m/year. This area of thick ice contained relatively few surge crevasses compared to the rest of Bering's trunk (Trantow & Herzfeld, 2018).

Burgess et al. (2013) observed that the surge appeared to subside between the initial acceleration in 2008 (initial surge phase) and the reinitiation in 2011 (second surge phase). Our simulation here, however, shows that while the surge kinematic wave continues to progress down glacier, ice-surface speeds will lessen when propagating through the thick ice between km-110 and km-125.

In addition, we also observe similar spatial velocity patterns in Bering's trunk between our modeled velocities and the maps produced by Burgess et al. (2013) for 2010.

Burgess et al. (2013) labels the areas of high velocity in Central Bering as "surge fronts", however, our model shows that these spatial patterns are persistent across the surge phase. The assumed surge fronts in Figure 3 of Burgess et al. (2013) are transposed on our modeled velocity map in Figure 11(b). Our results indicate that these high-velocity areas in Central Bering are not associated with surge fronts but are rather attributed to particulars of the local bedrock topography.

Near the end of the simulation, when the surge front has reached km-125, peak modeled velocities begin to once again increase, reaching maximums near 10 m/day (excluding modeled velocities in the overflow area, which are likely unrealistic). The modeled peak velocities in this area are consistent with those derived from the velocity map presented in Trantow and Herzfeld (2018). The simulation ends as the surge wave reaches the final reservoir area near km-128 approximately 2 years after surge initiation.

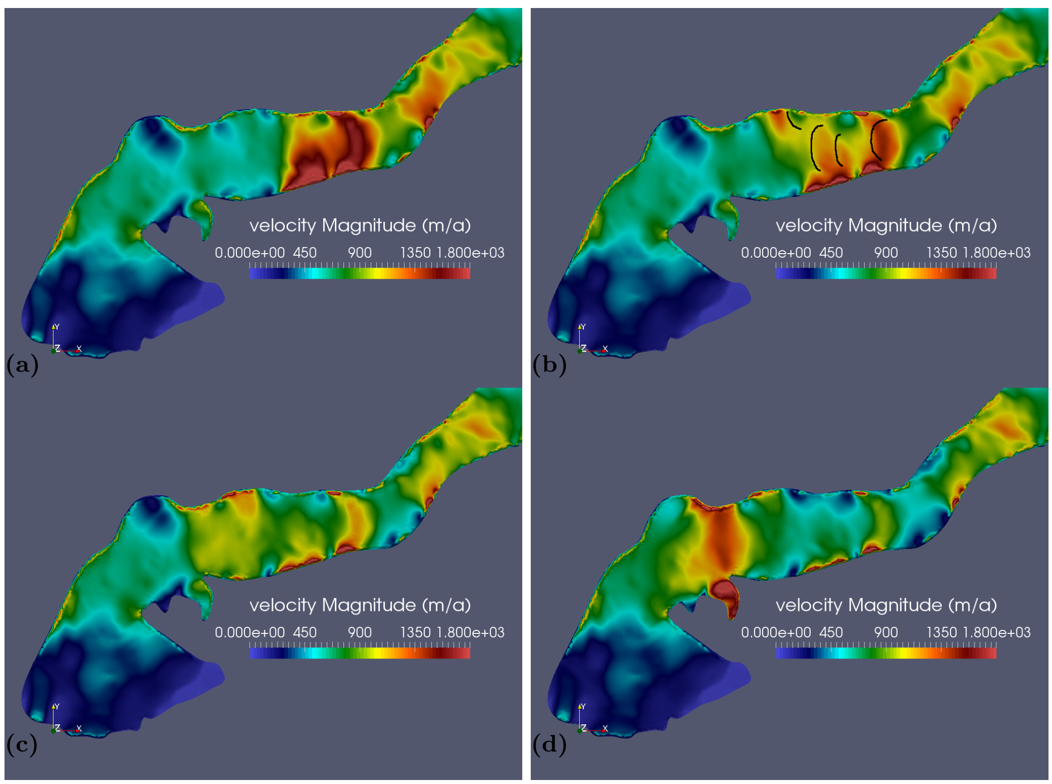

Figure 11. Modeled surface velocity throughout a short surge simulation. Velocity given in meters per year. (a) Velocity at time step 10, (b) velocity at time step 40 with the "surge fronts" assumed by Burgess et al. (2013) marked in black, (c) velocity at time step 80 and (d) velocity at time step 132.

5.2.2 Basal Shear Stress

Figure 12 gives the modeled basal shear stress (in the x, or along-flow, direction) at the same time stamps above. The surge front is clearly marked in each subfigure as a dividing line between low basal shear stresses up-glacier (white/yellow) and high basal shear stresses down-glacier (orange/red) of the surge front. This figure reveals that basal shear stresses are reduced far up-glacier, well above the initiation location at km-100, where quiescent basal friction parameters still apply. This result reflects observations of a surge wave that propagates down-glacier also having effects that propagate up-glacier into regions that are necessarily affected by local changes in basal drainage characteristics.

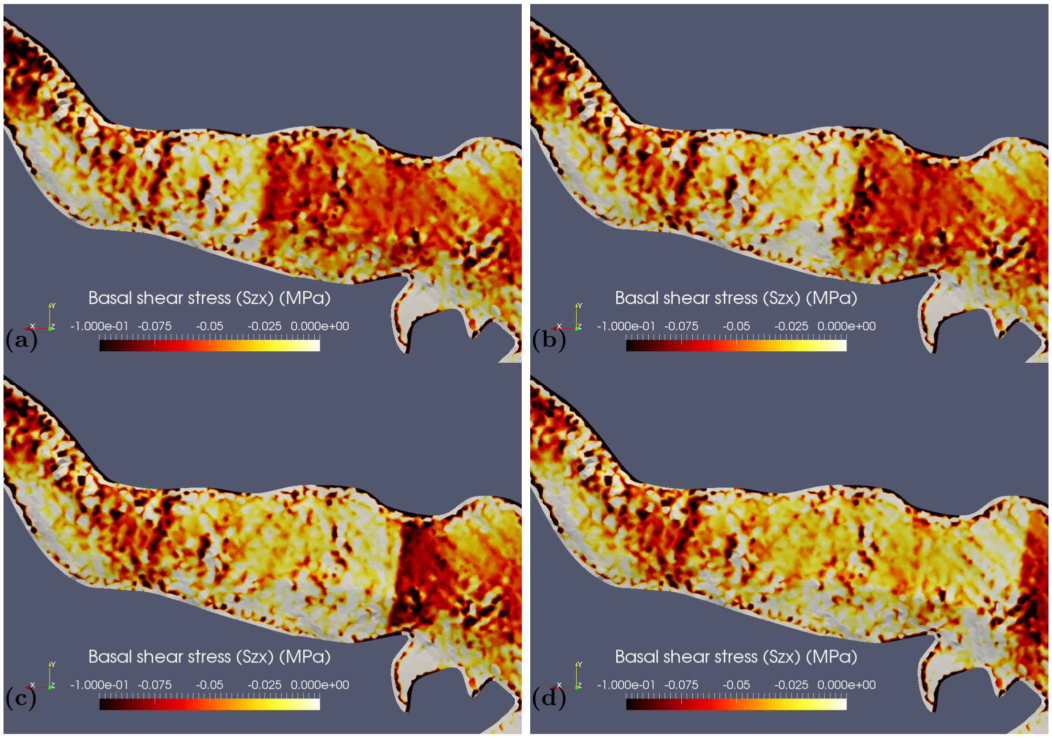

Figure 12. Modeled basal shear stress throughout a short surge simulation. Displayed is the basal shear stress that acts on the plane orthogonal to the z-axis in the direction of the x-axis. Note that we are viewing the glacier from the bottom, with the positive x-axis pointing to the left, unlike the other figures in this section where the glacier is viewed from above with the positive x-axis pointing to the right. Stress is given in units of mega-Pascals. (a) Basal shear stress at time step 10, (b) basal shear stress at time step 40, (c) basal shear stress at time step 80 and (d) basal shear stress at time step 132.

5.2.3 Elevation Change

Figure 13 shows elevation change throughout the surge simulation. Subfigure (a) gives the overall mass transfer near the beginning of the surge simulation to the end. In general, we see mass transfer from the upper trunk to the lower trunk, that is, from the areas affected by the surge to the down-glacier areas not yet affected (in terms of basal friction). We see elevation changes that exceed 50, and even 100 m, over the course of approximately 1 year, which is consistent with observations (U. C. Herzfeld et al., 2013; Burgess et al., 2013; Trantow & Herzfeld, 2016). Subfigure (b) gives the elevation change from time step 32 to time step 80, which shows that initial surface lowering in the activation zone ($\approx$3.9-4.0 $\times 10^5$ UTM-East) is larger than at the end of the surge simulation when ice from further up-glacier flows into the evacuated region. Notably, we see that there are significant elevation changes far down glacier of the active region indicating that regions away from the active surge zones are affected by the increased flow speeds long before the surge front reaches that area. Finally, subfigure (c) gives the elevation change from time step 80 to time step 132. This figure shows that surface lowering only occurs in the down-glacier half of the activation zone ($\approx$ 3.75-3.95 $\times 10^5$ UTM-East) where surge speeds are the largest. The mass transfer to upper Bering comes from the lower

Bagley Ice Field, across the BBJ, which relives the mass-build up of that area (RA-64). Perhaps most notably, at each moment in time the location of the surge front is obvious when looking at temporally-local elevation changes where the surface is actively lowering behind the front and raising in front of it, which would resemble the oft identified "surge bulge". We find that the overall spatiotemporal progression of elevation-change during the surge matches the observations derived from CryoSat-2 data as described in Trantow and Herzfeld (2016).

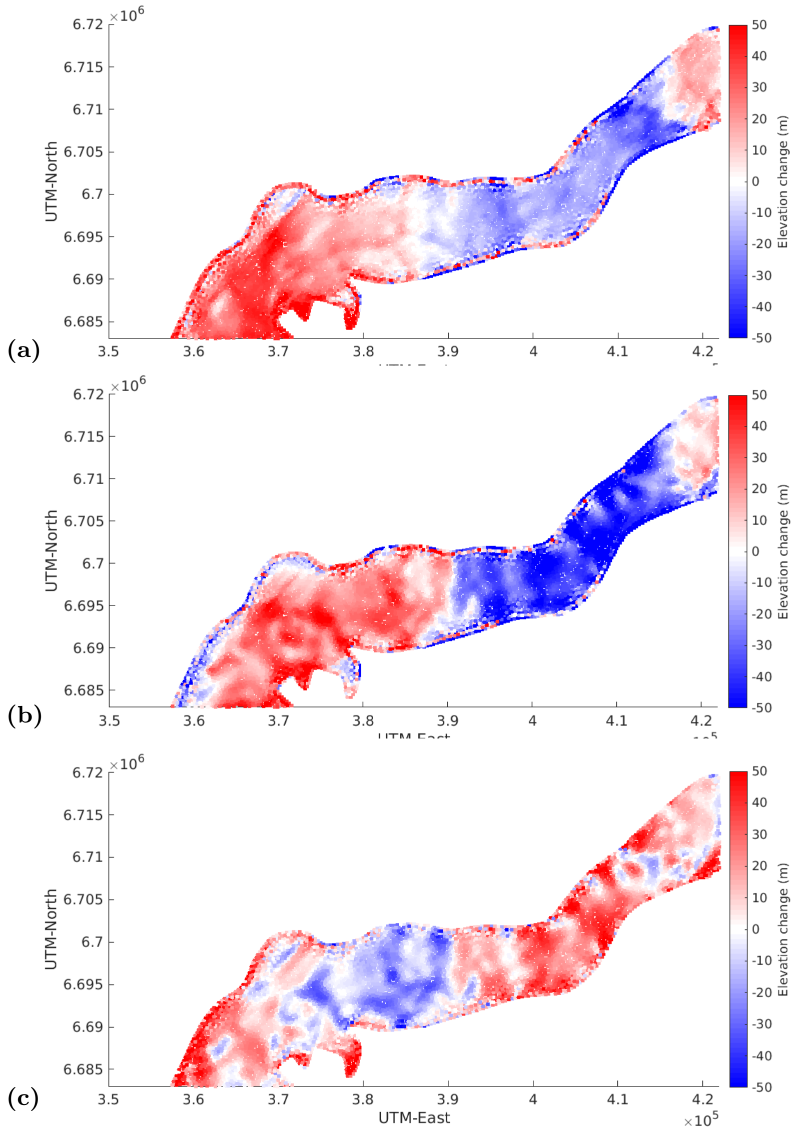

Figure 13. Modeled elevation change throughout a short surge simulation. Elevation change is given in units of meters. (a) Elevation difference between time 32 and time 132, (b) elevation difference between time 32 and time 80 and (c) elevation difference between time 80 and time 132.

5.2.4 Hydropotential

Finally, we take a look at the changing hydropotential and hydropotential gradient along-flowline during the surge simulation. Figure 14 shows these quantities near the beginning of the surge (after time step 32, a half-year into the initial surge phase) and in the middle of the initial surge phase after the surge front has progressed 20 km down-glacier (time step 80 or Day-400 of the initial surge phase). The first aspect to note is the change in hydropotential in the surge activation zone (km-100 to km-120). The hydraulic gradient has decreased throughout most of the activation zone implying that the passing surge wave, and the fast-sliding activation zone behind it, serves to further degrade the efficiency of the basal drainage system.

Previous theories predict that the passing of the surge (or kinematic) wave would activate the switch from an EDS to an IDS (W. B. Kamb, 1987). However, we show here, and in the previous section, that the basal drainage system becomes less efficient throughout quiescence and becomes even more inefficient once the surge wave passes through. Our approach also does not require any assumption of a linked-cavity system. We also see that the small ($\sim$3km) region centered at km-103 of positive hydraulic gradient, where water is predicted to collect, has shifted slightly down-glacier (indicated by an arrow in Figure 14(b)). This results implies that water accumulation areas may shift during the progression of the surge.

We also note that in the region up-glacier of the initiation location, the hydropotential "levels-out" with less variation along-flowline and a reduction in the estimated amount of basal water collection. This observation indicates that regions far up-glacier of the activation zone, which are modeled using the normal flow friction law value β_q, are becoming more efficient in their basal drainage indicating a return to a quiescent state as mass is redistributed down-glacier during the surge.

5.3 Second Surge Phase Analysis via Satellite Observations

In this section, we use CryoSat-2 DEMs to derive observation-based hydropotential maps of the BBGS during the 2011-2013 phase of the surge in order to infer drainage characteristics throughout the glacier during the peak of the surge in early-2011, when glacier velocities exceeded 22 m/day (Figure 15 (a)), and near the end of the surge in 2013 when dynamic activity in Bering Glacier had reduced significantly (Figure 15 (b)), with velocities below 2 m/day in most of Lower and Central Bering. These velocity maps are derived using feature-tracking methods applied to Landsat-7 and Landsat-8 imagery respectively. As seen in the early 2011 map, reliable velocity estimates are difficult to attain while the glacier is surging, with features used in correlation rapidly deforming over the course of several days (Trantow & Herzfeld, 2018). Moreover, the stripping in Landsat-7 imagery (Markham et al., 2004) greatly reduces the area for which ice-velocities can be derived. The Landsat-8 imagery used in the 2013 map, together with the glacier moving much slower, provides better overall velocity estimates for the BBGS. We note however, that the Sentinel-1 SAR imagery, available beginning in 2014, provide the most reliable and comprehensive velocity estimates (e.g., Figure 10(a)) due to the fact that SAR imagery is not complicated by the presence of clouds.

The CryoSat-2 satellite began providing reliable glacier height measurements around the start of the 2011-phase of the BBGS surge. As shown in Trantow and Herzfeld (2016), we can derive ice surface DEMs, and thus unique hydropotential maps, every six months from the CryoSat-2 data. Therefore, we can estimate hydropotential based on CryoSat-2 surface elevation observations rather than from modeled BBGS surface height as we have done previously. Figures 15(c) and (d) compare the CryoSat-2-estimated basal hydropotential for Summer 2011 (May 2011-October 2011) during the main acceleration phase and Summer 2013 (May 2013-October 2013) once most of the major surge activ-

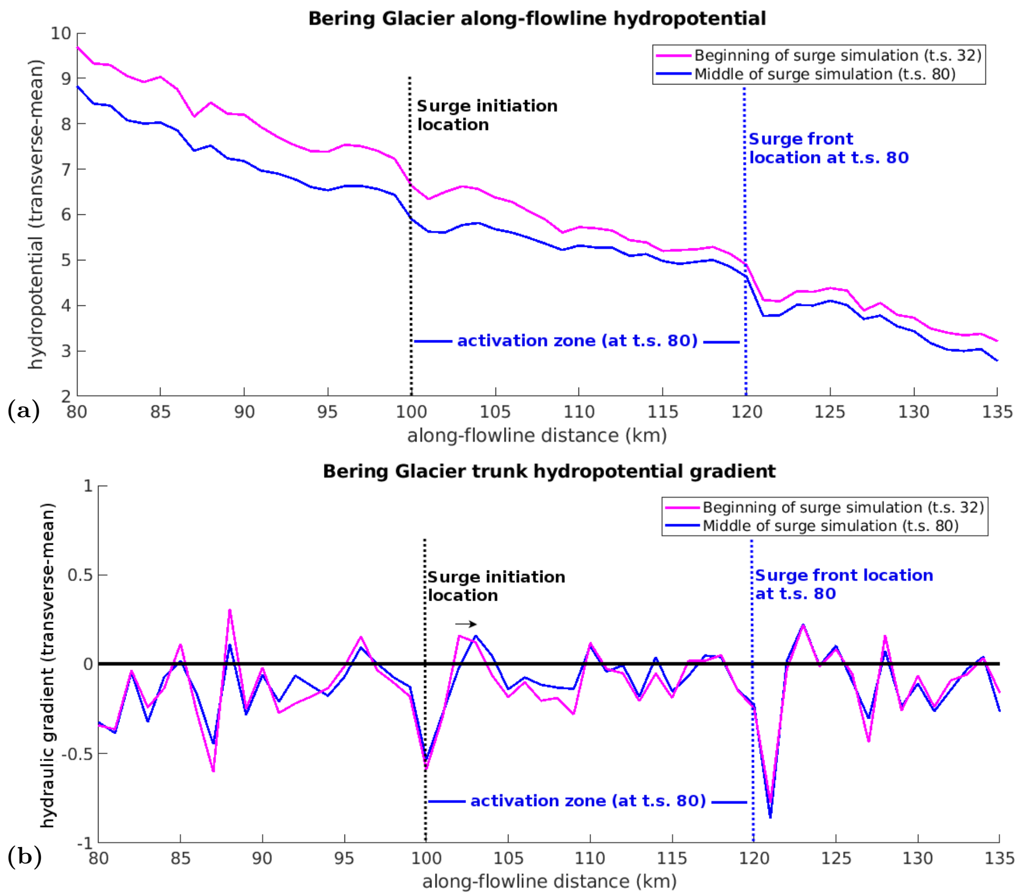

Figure 14. Hydropotential and hydraulic gradient during the surge simulation. The magenta curves correspond to the glacier state near the beginning of the surge at time step 32 (Day-160) and the blue lines correspond to the glacier state after the surge wave has propagated 20 km down-glacier at time step 80 (Day-400). Labeled are the surge initiation location along-flowline (black dotted line) and the surge front location along-flowline at time step 80 (blue dashed line). (a) Modeled hydropotential (MPa) and (b) modeled hydraulic gradient ($\frac{MPa}{km}$). The small black arrow indicates the shift of a water accumulation zone down-glacier during the surge.

ity in Bering Glacier had ceased. In Summer 2013, the hydropotential begins to better resemble the bed topographical potential and becomes less dominated by ice over burden pressure, with less water dispersing transversely and increased water drainage efficiency down-glacier. Looking at Bering Glacier's trunk, we see the contour lines become more evenly spaced and more transversely aligned in 2013. This indicates that a more steady, down-glacier flow, i.e. efficient flow, has manifested after the surge had ended by 2013 (in Central-Bering Glacier). We also see a reduction in the amount of hydropotential wells throughout the trunk indicating less capacity to store water beneath the glacier by the end of the surge.

These observations suggest that the transition from an IDS to an EDS begins at the glacier terminus, sometime between 2012 and 2013, and propagates up-glacier until it reaches the Bering-Bagley junction. The up-glacial surface velocity slowdown in the assumed IDS regions during this time indicate that the down-glacier EDS is more efficiently draining the up-glacial IDS, thus reducing basal water pressures there. Though,

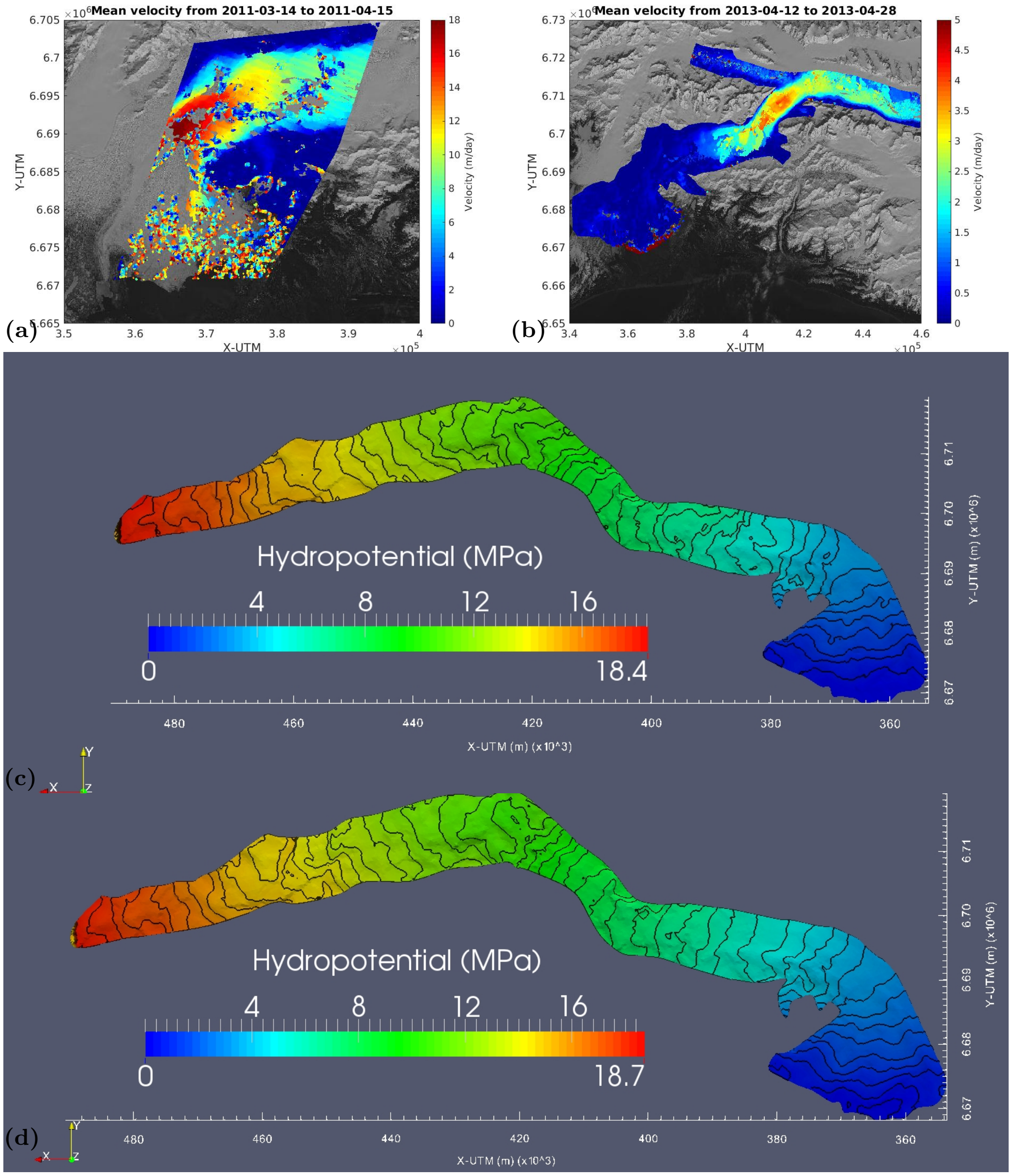

Figure 15. Velocity and basal hydropotential derived from observations during and after the surge in Bering Glacier. (a) Mean ice-surface velocity between 2011-03-14 and 2011-04-15 derived from Landsat-7 imagery. (b) Mean ice-surface velocity between 2013-04-12 and 2013-04-28 derived from Landsat-8 imagery. (b) Hydropotential derived from CryoSat-2 Baseline-C DEM for Summer 2011 (May 2011 - October 2011). (c) Hydropotential derived from CryoSat-2 Baseline-C DEM for Summer 2013 (May 2013 - October 2013). In conjunction with CryoSat-2 surface maps, both maps use the JPL-WISE bed topography maps in their estimation of hydropotential.

as we have shown in previous sections, the transition from an EDS to an IDS throughout quiescence is gradual and the drainage state is not simply binary. Therefore, we should expect the transition back to drainage efficiency to be somewhat gradual.

5.4 Observed Transition Back to Quiescence

In theory, after redistribution of mass throughout the glacier system, the glacier returns once more to a stable geometry. Slowdowns in the Alaskan-type surge-glacier systems are usually correlated with large outburst floods at the glacier terminus (W. Kamb et al., 1985), and the subglacial drainage system returns to an efficient one. This transition typically begins at the front of the glacier and slowly moves up-glacier until the entire glacier system returns to an EDS. This process is reflected by observed velocity at the cessation of the surge. The derived velocity map in Figure 15(b) from 2013 shows that low velocities (less that 1 m/day) exist in Lower Bering while higher velocities (2-5 m/day) remain in Upper Bering and the Bagley Ice Field. From 2012 onwards, the region of fast flow shrinks to only the Bagley Ice Field, with peak velocities also decreasing (Trantow, 2020). The highest velocities in 2013 remain in the Bagley Ice Field and just below the Bering-Bagley junction where basal slopes are high. By the year 2016, the entire glacier system is moving at less than 1 m/day, and effects of the recent surge have disappeared entirely, with the whole system in a state of low basal pressures and efficient drainage (Figure 10(a)).

6 Summary and Conclusions

In this paper, we utilized numerical simulations, supplemented by satellite and airborne observations, to investigate dynamic, geometric and hydraulic aspects of both the quiescent and surge phases of the Bering-Bagley Glacier System, Alaska. The analysis centers on inter-annual changes of mass redistribution throughout the glacier system and its implications on water drainage via calculation of hydropotential.

The quiescent phase simulation shows a steepening of local geometry, retainment of water and slowed-drainage paths that build throughout Bering Glacier's trunk leading to prime surging conditions. These results are mostly attributed to the particular properties of the bedrock topography. The most significant features are a series of subglacial ridges, which are extensions of the surrounding mountains beneath the glacier. These subglacial ridges lead to damming of ice and water over the course of quiescence. The build-up of ice at the subglacial ridges forms reservoir areas that slow down-glacier drainage in the areas directly up-glacier and can even lead to water retainment in the closest 2-4 km at several locations (specified in Figures 8 and 9). The simulation of the quiescent phase shows an increase of stored water in Bering Glacier's trunk by a factor of 2.46 over 20 years of evolution, which is estimated by calculating the positive hydraulic gradient area (shaded regions in Fig 8).

Moreover, the changing geometry during quiescence slows the overall down-glacier drainage through Bering Glacier's trunk through increased transverse water paths caused by the various ice dams. The difference in hydropotential across Bering's trunk, from km-80 to km-135, decreased 16.6% after 20 years of quiescent flow. The increasing amount of stored water and slowed down-glacier drainage lead to evermore water in the subglacial drainage system at a given time leaving the glacier primed for surging. While surge and quiescent phases are modeled in separate simulations, we propose a surge initiation criterion that is based on the inferred amount of stored water based on the hydropotential calculation.

Based on an observed surge wave in the BBGS, we propose a surge-wave friction law to simulate the initial surge phase through Bering Glacier's main trunk. Modeled velocities were consistent with those observed during the early stages of the latest surge in the BBGS from 2008 through 2010. Our results show that while changes in basal conditions are initially concentrated within an activation zone, as prescribed by the evolving friction law, significant basal shear stress and elevation changes occur throughout the glacier system indicating that effects from an initial surge acceleration can be seen to propagate both up- and down-glacier of the surge initiation area.

As the simulated surge front moves down-glacier, we find that the drainage efficiency further decreases within the active surging area. Glacier geometry begins to level out after ice in the reservoir areas is transferred to the receiving areas. Analysis of hydropotential maps, derived from CryoSat-2 altimeter data, indicates that the drainage system of the BBGS shows characteristics of a return to an efficient drainage system, where down-glacier flow dominates and hydropotential wells disappear.

In summary, our model of the BBGS captures key characteristics of the surge cycle including peak velocities, building reservoir areas and mass transfer. The bedrock topography DEM is an important component of the model's ability to capture observed spatial qualities of the glacier dynamics such as locations of reservoir areas and velocity patterns. Model physics were kept relatively simple as a first order attempt to recreate observed surge behaviors and we have proposed places where increased complexity could improve modeled results. This includes utilization of the hydropotential estimates for improving the uniform liner friction law used in quiescence, and also the surge-wave friction law.

7 Open Research

The Solver Input Files (SIF) for the Elmer/Ice simulations performed in this analysis, along with the Bering Glacier specific datasets and User Functions (USF), are available in the first author's GitHub repository:
`https://github.com/trantow/bbgs_elmer`.

Sentinel-1 SAR data are freely available at the Copernicus Open Access Hub:
`https://scihub.copernicus.eu/`

The Sentinel Application Platform (SNAP) (Veci et al., 2014), used in this project to derive velocity maps, is also freely available for download at:
`https://step.esa.int/main/download/snap-download/`

Acknowledgments
We would like to thank Dr. Ralf Greve (Institute of Low Temperature Science, Hokkaido University, Sapporo, Japan) for his invaluable input in our understanding of ice-dynamic modeling and for co-advising the first author in the research pertaining to this paper. We thank Eric Rignot (Jet Propulsion Laboratory, Pasadena, USA and University California Irvine, USA) and Jeremie Mouginot (University California Irvine, USA) for sharing their bed topographic data of the BBGS and Veit Helm (Alfred Wegener Institute, Bremen, Germany) for sharing their CryoSat-2 TFMRA-swath data for the BBGS. Support of this research through the U.S. National Science Foundation's Office of Polar Programs (Awards OPP-1745705 and OPP-1942356), Office of Advanced Cyberinfrastructure (Award OAC-1835256), Arctic Natural Sciences Program (Award ARC-1148800) and Geography and Spatial Sciences (Award GSS-1553133), and through NASA Cryospheric Sciences (Award NNX17AG75G) is gratefully acknowledged (U. Herzfeld is the PI of all awards).

References

Benn, D., Fowler, A. C., Hewitt, I., & Sevestre, H. (2019). A general theory of glacier surges. *Journal of Glaciology*, *65*(253), 701–716.

Björnsson, H. (1974). *Explanations of jökulhlaups from Grímsvötn, Vatnajökull, Ice-*

land.

Björnsson, H. (1998). Hydrological characteristics of the drainage system beneath a surging glacier. *Nature*, *395*(6704), 771.

Boulton, G., Lunn, R., Vidstrand, P., & Zatsepin, S. (2007). Subglacial drainage by groundwater-channel coupling, and the origin of esker systems: part 1-glaciological observations. *Quaternary Science Reviews*, *26*(7-8), 1067–1090.

Brinkerhoff, D. J., Meyer, C. R., Bueler, E., Truffer, M., & Bartholomaus, T. C. (2016). Inversion of a glacier hydrology model. *Annals of Glaciology*, *57*(72), 84–95.

Burgess, E. W., Forster, R. R., Larsen, C. F., & Braun, M. (2013). Surge Dynamics on Bering Glacier, Alaska, in 2008–2011. *The Cryosphere*, *6*, 1251–1262.

Chu, W., Schroeder, D. M., Seroussi, H., Creyts, T. T., Palmer, S. J., & Bell, R. E. (2016). Extensive winter subglacial water storage beneath the Greenland Ice Sheet. *Geophysical Research Letters*, *43*(24), 12–484.

Clarke, G. K., Collins, S. G., & Thompson, D. E. (1984). Flow, thermal structure, and subglacial conditions of a surge-type glacier. *Canadian Journal of Earth Sciences*, *21*(2), 232–240.

Cuffey, K., & Paterson, W. S. B. (2010). *The Physics of Glaciers* (4th ed.). Elsevier.

de Fleurian, B., Werder, M. A., Beyer, S., Brinkerhoff, D. J., Delaney, I., Dow, C. F., ... others (2018). SHMIP The subglacial hydrology model intercomparison Project. *Journal of Glaciology*, *64*(248), 897–916.

Eisen, O., Harrison, W., Echelmeyer, K., Bender, G., & J.Gorda. (2005). Variegated Glacier, Alaska, USA: A century of surges. *Journal of Glaciology*, *51*, 399-406.

Fatland, D., Lingle, C., & Truffer, M. (2003). A surface motion survey of Black Rapids Glacier, Alaska, U.S.A. *Annals of Glaciology*, *36*, 29–36.

Fatland, D. R., & Lingle, C. S. (1998). Analysis of the 1993-95 Bering Glacier (Alaska) surge using differential SAR interferometry. *Journal of Glaciology*, *44*(148), 532–546.

Fatland, D. R., & Lingle, C. S. (2002). InSAR observations of the 1993-95 Bering Glacier (Alaska, USA) surge and a surge hypothesis. *Journal of Glaciology*, *48*(162), 439–451.

Fleischer, P. J., Bailey, P. K., Natel, E. M., Muller, E. H., Cadwell, D. H., & Russell, A. (2010). The 1993-1995 surge and foreland modification, Bering Glacier, Alaska. *Geological Society of America Special Paper*(462), 193–216.

Fleurian, B. d., Gagliardini, O., Zwinger, T., Durand, G., Meur, E. L., Mair, D., & Råback, P. (2014). A double continuum hydrological model for glacier applications. *The Cryosphere*, *8*(1), 137–153.

Flowers, G. E., & Clarke, G. (2002a). A multicomponent coupled model of glacier hydrology, 1, Theory and synthetic examples. *Journal Geophys. Res.*, *107*(B11), 2287. doi: 10.1029/2001JB001122

Flowers, G. E., & Clarke, G. (2002b). A multicomponent coupled model of glacier hydrology, 2, Application to Trapridge Glacier, Yukon, Canada. *Journal Geophys. Res.*, *107*(B11), 2288. doi: 10.1029/2001JB001124

Fowler, A. (1987). A theory of glacier surges. *Journal of Geophysical Research: Solid Earth (1978–2012)*, *92*(B9), 9111–9120.

Fowler, A. (1989). A mathematical analysis of glacier surges. *SIAM J. Appl. Math.*, *49*(1), 246-263.

Gagliardini, O., Zwinger, T., Gillet-Chaulet, F., Durand, G., Favier, L., Fleurian, B. d., ... others (2013). Capabilities and performance of Elmer/Ice, a new-generation ice sheet model. *Geoscientific Model Development*, *6*(4), 1299–1318.

Greve, R., & Blatter, H. (2009). *Dynamics of Ice Sheets and Glaciers.* Berlin, Germany etc.: Springer. doi: 10.1007/978-3-642-03415-2

Gulley, J., Benn, D., Screaton, E., & Martin, J. (2009). Mechanisms of englacial conduit formation and their implications for subglacial recharge. *Quaternary Science Reviews*, *28*(19-20), 1984–1999.

Gulley, J., Grabiec, M., Martin, J., Jania, J., Catania, G., & Glowacki, P. (2012). The effect of discrete recharge by moulins and heterogeneity in flow-path efficiency at glacier beds on subglacial hydrology. *Journal of Glaciology*, *58*(211), 926–940.

Harrison, W., & Post, A. (2003). How much do we really know about glacier surging? *Annals of Glaciology*, *36*(1), 1–6.

Heinrichs, T. A., Mayo, L., Echelmeyer, K., & Harrison, W. (1996). Quiescent-phase evolution of a surge-type glacier: Black Rapids Glacier, Alaska, USA. *Journal of Glaciology*, *42*(140), 110–122.

Helm, V., Humbert, A., & Miller, H. (2014). Elevation and elevation change of Greenland and Antarctica derived from CryoSat-2. *The Cryosphere*, *8*(4), 1539–1559.

Herzfeld, U. (1998). *The 1993-1995 surge of bering glacier (Alaska) — a photographic documentation of crevasse patterns and environmental changes* (Vol. 17). Geograph. Gesellschaft Trier and Fachbereich VI – Geographie/Geowissenschaften, Universität Trier.

Herzfeld, U. C. (2004). *Atlas of Antarctica: Topographic maps from geostatistical analysis of satellite radar altimeter data* (Vol. 1). Springer Verlag.

Herzfeld, U. C., & Mayer, H. (1997). Surge of Bering Glacier and Bagley Ice Field, Alaska: an update to August 1995 and an interpretation of brittle-deformation patterns. *Journal of Glaciology*, *43*(145), 427–434.

Herzfeld, U. C., McDonald, B., Stachura, M., Hale, R. G., Chen, P., & Trantow, T. (2013). Bering Glacier surge 2011: Analysis of laser altimeter data. *Annals of Glaciology*, *54(63)*, 158–170. doi: 10.3189/2013AoG63A348

Humphrey, N. F., & Raymond, C. (1994). Hydrology, erosion and sediment production in a surging glacier: Variegated Glacier, Alaska, 1982–83. *Journal of Glaciology*, *40*(136), 539–552.

Jay-Allemand, M., Gillet-Chaulet, F., Gagliardini, O., & Nodet, M. (2011a). Investigating changes in basal conditions of Variegated Glacier prior to and during its 1982-1983 surge. *The Cryosphere*, *5*(3), 659–672.

Jay-Allemand, M., Gillet-Chaulet, F., Gagliardini, O., & Nodet, M. (2011b). Investigating changes in basal conditions of Variegated Glacier prior to and during its 1982-1983 surge. *The Cryosphere*, *5*(3), 659–672. Retrieved from http://www.the-cryosphere.net/5/659/2011/ doi: 10.5194/tc-5-659-2011

Jiskoot, H. (1999). Characteristics of surge-type glaciers. *Ph.D. thesis*, 1-262.

Josberger, E. G., Shuchman, R. A., Meadows, G. A., Savage, S., & Payne, J. (2010). Hydrography and circulation of ice-marginal lakes at Bering Glacier, Alaska, USA. *Geological Society of America Special Paper*(462), 67–82.

Kamb, B. (1970). Sliding motion of glaciers: theory and observation. *Reviews of Geophysics*, *8*(4), 673–728.

Kamb, W., Raymond, C., Harrison, W., Engelhardt, H., Echelmeyer, K., Humphrey, N., ... Pfeffer, T. (1985). Glacier surge mechanism: 1982-1983 surge of Variegated Glacier, Alaska. *Science*, *227*(4686), 469-479.

Kamb, W. B. (1987). Glacier Surge Mechanism Based on Linked Cavity Configuration of the Basal Water Conduit System. *Journal Geophys. Res.*, *92*(B9), 9083-9100.

Koehler, R., & Carver, G. (2018). Active faults and seismic hazards in Alaska. *Alaska Div. Geol. Geophys. Surv., Miscellaneous Publication 160*.

Larour, E., Utke, J., Csatho, B., Schenk, A., Seroussi, H., Morlighem, M., ... Khazendar, A. (2014). Inferred basal friction and surface mass balance of North-East Greenland Ice Stream using data assimilation of ICESat-1 surface altimetry and ISSM. *The Cryosphere Discussions*, *8*(3), 2331–2373. Retrieved from http://www.the-cryosphere-discuss.net/8/2331/2014/ doi:

10.5194/tcd-8-2331-2014

Larsen, C., Burgess, E., Arendt, A., O'neel, S., Johnson, A., & Kienholz, C. (2015). Surface melt dominates Alaska glacier mass balance. *Geophysical Research Letters*, *42*(14), 5902–5908.

LeBlanc, L. (2009). *Icequakes and ice motion: A time-series analysis of the dynamics of the Bering Glacier, Alaska* (Unpublished doctoral dissertation). University of Alaska Fairbanks.

Lingle, C., & Fatland, D. (2003). Does englacial water storage drive temperate glacier surges? *Annals of Glaciology*, *36*, 14–20.

Lingle, C., Post, A., Herzfeld, U. C., Molnia, B. F., Krimmel, R., & Roush, J. (1993). Bering Glacier surge and iceberg-calving mechanism at Vitus Lake, Alaska, USA. *Journal of Glaciology*, *39*, 722–727.

Lliboutry, L. (1968). General theory of subglacial cavitation and sliding of temperate glaciers. *Journal of Glaciology*, *7*, 21–58.

Magnússon, E., Björnsson, H., Rott, H., & Pálsson, F. (2010). Reduced glacier sliding caused by persistent drainage from a subglacial lake. *The Cryosphere*, *4*(1), 13–20.

Markham, B. L., Storey, J. C., Williams, D. L., & Irons, J. R. (2004). Landsat sensor performance: History and current status. *IEEE Transactions on Geoscience and Remote Sensing*, *42*(12), 2691–2694.

Mayer, H., & Herzfeld, U. (2000). Structural glaciology of the fast-moving Jakobshavn Isbræ, Greenland, compared to the surging Bering Glacier, Alaska, USA. *Annals of Glaciology*, *30*(1), 243–249.

Meier, M., & Post, A. (1969). What are glacier surges? *Canadian Journal of Earth Sciences*, *6*(4), 807–817.

Molnia, B., & Post, A. (1995). Holocene history of Bering Glacier, Alaska: A prelude to the 1993-1994 surge. *Physical Geography*, *16*(2), 87–117.

Molnia, B., & Williams, R. (2001). *Glaciers of Alaska* (Vol. 28-2). Alaska Geographic Society.

Molnia, B. F. (2008). *Alaska*. Washington, D.C.: U.S. Geological Survey Professional Paper 1386-K.

Molnia, B. F., & Post, A. (2010). Introduction to the Bering Glacier system, Alaska/Canada: Early Observations and scientific investigations, and key geographic features. *Geological Society of America Special Paper*(462), 13–42.

Murray, T. (1997). Assessing the paradigm shift: deformable glacier beds. *Quaternary Science Reviews*, *16*(9), 995–1016.

Murray, T., Strozzi, T., Luckman, A., Jiskoot, H., & Christakos, P. (2003). Is there a single surge mechanism? Contrasts in dynamics between glacier surges in Svalbard and other regions. *Journal of Geophysical Research: Solid Earth*, *108*(B5).

Post, A. (1972). Periodic surge origin of folded medial moraines on Bering Piedmont Glacier, Alaska. *Journal of Glaciology*, *11*(62), 219-226.

Raymond, C. (1987). How do glaciers surge? A review. *Journal of Geophysical Research*, *92*(B9), 9121–9134.

Raymond, C. (1988). Evolution of Variegated Glacier, Alaska, USA, prior to its surge. *J. Glaciol*, *34*(117), 154–169.

Raymond, C., Benedict, R., Harrison, W., Echelmeyer, K., & Sturm, M. (1995). Hydrological discharges and motion of Fels and Black Rapids Glaciers, Alaska, USA: implications for the structure of their drainage systems. *Journal of Glaciology*, *41*(138), 290–304.

Raymond, C., Johannesson, T., Pfeffer, T., & Sharp, M. (1987). Propagation of a glacier surge into stagnant ice. *Journal of Geophysical Research: Solid Earth*, *92*(B9), 9037–9049.

Rignot, E., Mouginot, J., Larsen, C., Gim, Y., & Kirchner, D. (2013). Low-frequency radar sounding of temperate ice masses in Southern Alaska. *Geo-*

physical Research Letters, *40*(20), 5399–5405.
Robin, G. d. Q. (1969). Initiation of glacier surges. *Canadian Journal of Earth Sciences*, *6*(4), 919–928.
Robin, G. d. Q., & Weertman, J. (1973). Cyclic surging of glaciers. *Journal of Glaciology*, *12*(64), 3–18.
Roush, J. J., Lingle, C. S., Guritz, R. M., Fatland, D. R., & Voronina, V. A. (2003). Surge-front propagation and velocities during the early-1993-95 surge of Berring Glacier, Alaska, U.S.A., from sequential SAR imagery. *Annals of Glaciology*, *36*, 37–44.
Sevestre, H., Benn, D. I., Hulton, N. R., & Bælum, K. (2015). Thermal structure of Svalbard glaciers and implications for thermal switch models of glacier surging. *Journal of Geophysical Research: Earth Surface*, *120*(10), 2220–2236.
Sharp, M., Richards, K., Willis, I., Arnold, N., Nienow, P., Lawson, W., & Tison, J.-L. (1993). Geometry, bed topography and drainage system structure of the haut glacier d'arolla, switzerland. *Earth Surface Processes and Landforms*, *18*(6), 557–571.
Shoemaker, E. (1986). Subglacial hydrology for an ice sheet resting on a deformable aquifer. *J. Glaciol*, *32*(110), 20–30.
Shoemaker, E., & Leung, H. (1987). Subglacial drainage for an ice sheet resting upon a layered deformable bed. *Journal of Geophysical Research: Solid Earth*, *92*(B6), 4935–4946.
Shreve, R. (1972). Movement of water in glaciers. *Journal of Glaciology*, *11*(62), 205–214.
Shuchman, R., & Josberger, E. G. (2010). Bering Glacier: Interdisciplinary Studies of Earth's Largest Temperate Glacier. *Geological Society of America Special Paper*(462), 384.
Shuchman, R. A., Josberger, E. G., Jenkins, L. K., Payne, J. F., Hatt, C. R., & Spaete, L. (2010). Remote sensing of the Bering Glacier region. *Geological Society of America Special Paper*(462), 43–66.
Tangborn, W. (2013). Mass balance, runoff and surges of Bering Glacier, Alaska. *The Cryosphere*, *7*(3), 867–875.
Trantow, T. (2014). *Numerical experiments of dynamical processes during the 2011-2013 surge of the Bering-Bagley Glacier System, using a full-Stokes finite element model* (Unpublished master's thesis). University of Colorado.
Trantow, T. (2020). *Surging in the bering-bagley glacier system, alaska – understanding glacial acceleration through new methods in remote sensing, numerical modeling and model-data comparison* (Unpublished doctoral dissertation). University of Colorado.
Trantow, T., & Herzfeld, U. (2016). Spatiotemporal mapping of a large mountain glacier from CryoSat-2 altimeter data: surface elevation and elevation change of Bering Glacier during surge (2011-2014). *International Journal of Remote Sensing*, 0-28. doi: 10.1080/01431161.2016.1187318
Trantow, T., & Herzfeld, U. C. (2018). Crevasses as indicators of surge dynamics in the Bering Bagley Glacier System, Alaska: Numerical experiments and comparison to image data analysis. *Journal of Geophysical Research: Earth Surface*. doi: 10.1029/2017JF004341
Trantow, T., Herzfeld, U. C., Helm, V., & Nilsson, J. (2020). Sensitivity of glacier elevation analysis and numerical modeling to cryosat-2 siral retracking techniques. *Computers & Geosciences*, 104610.
Truffer, M., Harrison, W. D., & Echelmeyer, K. A. (2000). Glacier motion dominated by processes deep in underlying till. *Journal of Glaciology*, *46*(153), 213–221.
Turrin, J., Forster, R. R., Larsen, C., & Sauber, J. (2013). The propagation of a surge front on Bering Glacier, Alaska, 2001-2011. *Annals of Glaciology*, *54*(63).

Veci, L., Prats-Iraola, P., Scheiber, R., Collard, F., Fomferra, N., & Engdahl, M. (2014). The Sentinel-1 toolbox. In *Proceedings of the ieee international geoscience and remote sensing symposium (igarss)* (pp. 1–3).

Weertman, J. (1972). General theory of water flow at the base of a glacier or ice sheet. *Reviews of Geophysics*, *10*(1), 287–333.